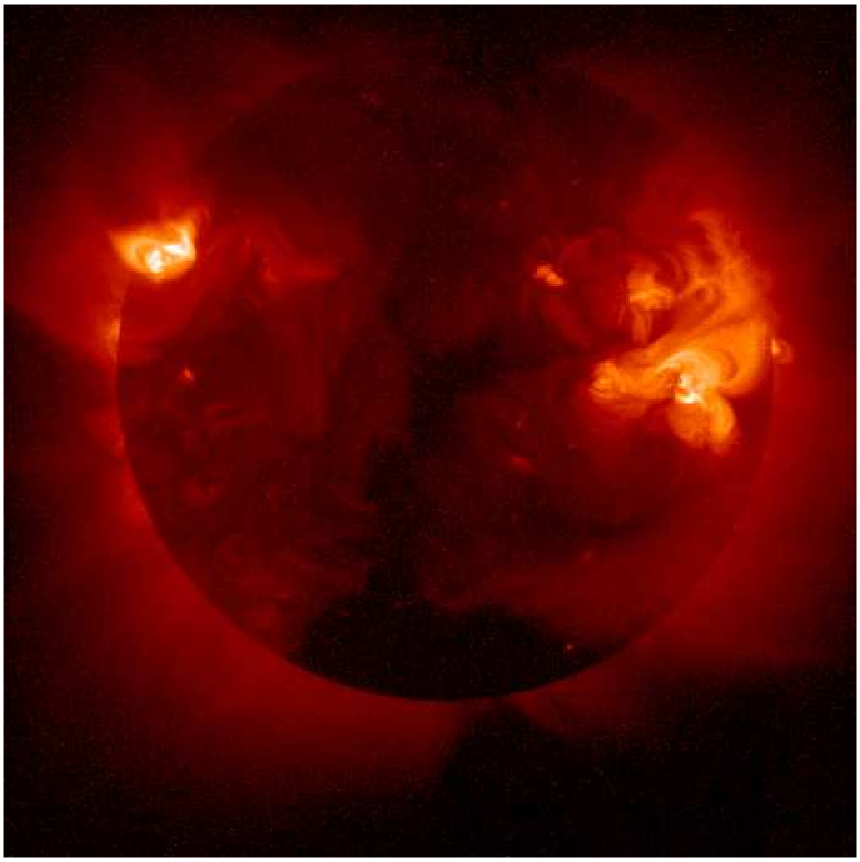

ROTATION PATTERNS IN THE LARGE-SCALE SOLAR CORONA

by

Mark Alan Weber

A thesis submitted in partial fulfillment
of the requirements for the degree

of

Doctor of Philosophy

in

Physics

MONTANA STATE UNIVERSITY — BOZEMAN
Bozeman, Montana

December 1999

APPROVAL

of a thesis submitted by

Mark Alan Weber

This thesis has been read by each member of the thesis committee, and has been found to be satisfactory regarding content, English usage, format, citations, bibliographic style and consistency, and is ready for submission to the College of Graduate Studies.

Dana W. Longcope, Ph. D. ____________________ __________
(Signature) Date

Approved for the Department of Physics

John C. Hermanson, Ph. D. ____________________ __________
(Signature) Date

Approved for the College of Graduate Studies

Bruce R. McLeod, Ph. D. ____________________ __________
(Signature) Date

STATEMENT OF PERMISSION TO USE

ACKNOWLEDGEMENTS

Sennichi no kingaku yori ichi nichi no meishō: "Better than a thousand days of diligent study is one day with a great teacher."

— Japanese proverb

I have had the good fortune to benefit from great teachers as well as ample studies. There is insufficient room here to recognize all of the people who have assisted my dissertation with their kindness, yet an effort should be undertaken.

As my thesis advisor, Dana Longcope provided guidance with a light but deft touch that encouraged professional self-direction while keeping me on the general course. Of equal importance was Loren Acton, who admitted me to the nascent Solar Physics Group at MSU and supervised my early research, and who always has been willing to share his sound viewpoint on matters professional, scientific, or otherwise.

At MSU, my knowledge of solar physics and experience of scientific collaboration was greatly extended by the other members of the Solar Physics Group: Piet Martens, Richard Canfield, David Alexander, Alexei Pevtsov, Charles Kankelborg, David McKenzie, and especially Brian Handy, who set the precedent and showed me how the solar physics thesis thing is done. I want to thank William Hiscock, for his understanding and support, and Richard Robiscoe, for being the physics professor we all admire and wish to be like when we grow up.

I acknowledge the input of co-authors on my papers: Loren Acton, David Alexander, H. Hara, S. Kubo, Dana Longcope, and Piet Martens. My research also benefitted from discussions with and support from Jack Harvey, Robert Howard, Hugh Hudson, and Peter Sturrock. Also, Taeil Bai introduced me to the useful device of stackplots. I would also like to say a special thank you to Prof. Y. Ogawara and the many people on the *Yohkoh* project at the Japanese Institute of Space and Astronautical Science and at the Lockheed-Martin Solar and Astrophysics Laboratory who gave me a wonderful opportunity to participate in and contribute to leading-edge observations of the Sun. *Yohkoh* is a mission of the Japanese Institute for Space and Astronautical Science. The MSU work is supported by NASA under contract NAS8-37334. Additionally, I was supported in part by a Montana Space Grant Fellowship through the Montana Space Grant Consortium Federal Grant NGT-40041, and by a departmental scholarship from the Seifert family.

Frontispiece A full-disk composite image of the Sun taken by *Yohkoh*/SXT on March 12, 1993 at 10:21 UT. The south polar coronal hole extension for Carrington Rotation 1866 can be seen.

TABLE OF CONTENTS

LIST OF TABLES

LIST OF FIGURES

ABSTRACT

The work presented in this thesis is composed of three research topics organized around the theme of solar differential rotation. The first section presents a method for reconstructing the presence of multiple, yet differing, rotation signals. The Soft X-ray Telescope (SXT, Tsuneta et al. 1991) onboard the Japanese satellite *Yohkoh* takes images of the solar corona. The corona is highly structured by the solar magnetic field, and with an instrument range of six orders of magnitude, many features are discernable in the SXT data. Some features persist for several solar rotations and so it is possible to analyze the data at a particular latitude as a time-series modulated at the period of the solar rotation. The Lomb-Scargle periodogram is used iteratively to extract the most significant frequency components from time-series made of SXT data. The variance of the set of extracted signals is interpreted as the variance of rotation signals on the Sun, and gives positive results above the $1\,\sigma$ level of the independently estimated uncertainty. The method is shown to reproduce mean rotation profiles versus latitude which agree with the results from the more traditional autocorrelation method.

The next section introduces the observation that the rotation rate of high latitudes in the southern solar hemisphere during the last activity cycle exhibited bimodal behavior with relatively abrupt transitions. This behavior reflected the evolution of a large region of unipolar flux underlying a coronal hole. Using the flux-transport model, developed mostly by Sheeley, Nash, and Wang (SNW) and which incorporates surface flows like the solar differential rotation, this behavior is reproduced with a zonal approximation. It is shown that the mode identity is determined by the presence or absence of an "active longitude"– an area where concentrated flux repeatedly erupts through the surface for several solar rotations. This result adds to the discussion on the influence of the flux source function in the SNW description.

The last section explores the role of the solar differential rotation in producing coronal structures called "prominences". For a prominence model to produce magnetic fields with axial components which obey a hemispheric rule observed on the Sun is problematic. One solution posed by van Ballegooijen & Martens (1990) involves a reorientation of the structure through a large angle ($\gtrsim 90^\circ$), but was deemed implausible for lack of observational support. Chapter 4 points out that prominence structures are generally thought to be formed from the remnant fields of decaying active regions, which (statistically) start with the correct orientation according to "Joy's Law".

CHAPTER 1

INTRODUCTION

The discovery that the surface of the Sun rotates differentially with latitude occurred about three hundred years ago from observations of the passage of sunspots across the solar disk. In the nineteenth century, Richard Carrington made measurements showing that the solar rotation is fastest at the equator and decreases towards the poles, i.e., it rotates differentially. Since then, many different methods have been devised to probe various features and layers of the Sun, and these observations have revealed that the rotation varies not only with latitude, but also with depth and among types of features.

In conjunction with the solar magnetic field, differential rotation plays a key role in the active life of the Sun. Rotational gradients at the base of the convective zone power a dynamo mechanism which completely regenerates the solar magnetic field every eleven years. The field there is buoyant to perturbations and rises to the surface in flux bundles. "Active regions" and sunspots occur where these field concentrations erupt through the photosphere; their subsequent evolution often give rise to all sorts of active phenomena, ranging from flares in the Hα and optical wavelengths to coronal mass ejections and particle storms at 1 a.u.

The flux concentrations eventually disperse, and their motion can be well-described by transport flows at the photosphere; the differential rotation turns out to be a significant influence in this respect as well. Because of the high electrical conductivity of the solar atmosphere, observable features such as active regions (which are so hot they emit thermal radiation at soft x-ray wavelengths) reflect the magnetic field structure above the photosphere, so their evolution largely follows the surface motions of the flux. As a consequence, the differential rotation at the surface layers is important to understanding most of the large-scale behavior of the observable Sun.

This dissertation is primarily comprised of three sections which explore the role of differential rotation in observable solar phenomena. In Chapter 2, differential rotation rates of soft X-ray features in the solar corona are investigated. The rotation profile is quantified by a method of harmonic filtering using the Lomb-Scargle Periodogram. This approach leads reasonably to a quantitative discrimination between uncertainty estimates and spectral leakage of the fundamental rotation frequency due to the presence of multiple rotating tracers. Mean rotation rates as a function of latitude and year are calculated for the years 1992–1997 (roughly the declining phase of the last solar activity cycle). The corona is found to have a small but measurable latitudinal gradient in rotation rate. The presence of multiple features places a lower bound of 1–2% on the relative uncertainties with which a "mean" rotation rate can be measured. The results are compared with autocorrelation estimates and found to agree within

1σ.

Chapter 3 presents the discovery that, during the early declining phase of the previous solar activity cycle (no. 22), the south polar coronal hole extension alternated between two modes characterized by their width and rotation rate. This behavior is understandable in the context of a description of unipolar magnetic regions according to a flux transport model developed by Sheeley, Nash and Wang (SNW). The flux transport equations are solved using a measured source function as input. Results are shown to reproduce the two observed modes; one of the modes is demonstrated to be a consequence of the presence of an "active longitude". These results provide a caveat to the SNW discussion of the impact of flux sources on unipolar magnetic flux regions.

The formation of poleward-migrating coronal magnetic structures associated with high-latitude solar prominences is considered in Chapter 4. These structures are observed to have axial fields which are inconsistent in direction with models in which differential rotation acts upon a line-tied, coronal magnetic field along a polarity inversion line running east-west. Van Ballegooijen and Martens (1990) pointed out that the correct axial fields are produced when the polarity inversion line begins at a large tilt angle ($\gtrsim 90°$) with respect to latitude, but considered this mechanism to be implausible for solar prominences. This chapter argues that decaying active regions provide the regions of unipolar flux between which prominences are observed to form, and demonstrates how "Joy's Law" provides a range of initial tilt angles for axial fields to be formed with the correct orientation.

CHAPTER 2

CHARACTERIZING ROTATION RATES IN THE SOFT X-RAY CORONA

2.1 Introduction

The rotation of the solar corona is a subject of some interest, particularly insofar as the latitudinal dependence appears to deviate from that of the underlying photosphere. While there have been many studies of coronal differential rotation, through both observation (e.g., white-light K-corona: Hansen, Hansen, & Loomis 1969; Fisher & Sime 1984; Fe XIV "green-line": Sime, Fisher, & Altrock 1989; Wang et al. 1997; and microwaves: Aschwanden et al. 1995) and extrapolation of photospheric data (e.g., Hoeksema 1984; Hoeksema & Scherrer 1987; and Wang et al. 1988), the potential of soft X-ray (SXR) data has yet to be fully exploited. Some initial work in this direction includes the *Skylab* observations of apparently rigidly rotating coronal holes (Timothy, Krieger, & Vaiana 1975) and an early application of *Yohkoh* data (Kozuka et al. 1994). Presently, however, the *Yohkoh* database extends over a half an activity cycle, providing an unprecedented opportunity to study temporal and spatial variations in the SXR rotation rates. Also, the *Yohkoh* Soft X-Ray Telescope (SXT; Tsuneta et al. 1991) provides data of a higher quality than was possible at the time of *Skylab*.

Like emission-line data, the solar SXR emission is dependent upon both the plasma temperature and density. Sime, Fisher, & Altrock (1989) conjectured that the Fe XIV signal describes the convolution of local heating centers with overlying density structures; the SXR data could provide complementary insight in a further investigation of this possibility. Unlike an emission-line study, however, the SXT is a broadband instrument which is capable of simultaneously observing and identifying active regions, "quiet corona"[1], and coronal holes (i.e., tracers of the SXR signal) in an unambiguous way. Furthermore, the broad temperature response of the SXT, as opposed to relatively narrow response in emission-line observations, mitigates against the acquisition or loss of features because of temperature changes (although it should be mentioned that the SXT response is biassed towards higher temperatures). This ability to make a direct association between components of the SXR signal and various structures of the solar atmosphere facilitates the understanding of the emergence and evolution of subsurface magnetic flux, as well as the organization of the interplanetary magnetic field (IMF) and solar wind.

Previous studies of coronal structures indicate that larger-scale features can persist for several synodic rotations (cf., Fisher & Sime 1984), and perusal of stackplots made from SXT images supports this observation (Figure 2.1). Indeed, light curves

---

[1] Here, "quiet corona" is used to denote the diffuse, unresolved, non-active region emission seen by the *Yohkoh*/SXT.

made of the solar SXR emission show a clear modulation which can be readily attributed to the rotation of various identifiable and persistent tracers across the visible hemisphere. Traditionally (e.g., Hansen, Hansen, & Loomis 1969), the persistence of such tracers has been used to justify the application of the autocorrelative method to produce a characteristic rotation rate for the data. However, the multicomponent corona can display several different rotation rates over timescales comparable to the lifetime of a tracer feature, as evidenced in Figure 2.1. The method of partial spectral decomposition developed in this paper is an attempt to utilize spectral analysis to describe the significant component rates of the coronal rotation signal, using irregularly sampled data. In this paper, synoptic observations of spatially resolved SXR emission are converted to time-series, which are then analyzed for harmonic content by what is essentially least-squares fitting. The time-series are considered to have three types of components: (a) a characteristic rotation signal (to be operationally defined in Equation (2.9)), (b) perturbations on timescales comparable to the tracer lifetimes (months), and (c) perturbations on short timescales comparable to the sampling rate (an hour). The data variance associated with the second case is ascribed to gradual evolutions and variances in the amplitudes, phases, and durations of the tracer signals, and an estimate of this variance is used to characterize the "actual" spread of rotation rates among the coronal features over the course of a year. The third case is used to estimate the measurement uncertainty of individual data values, and thus place uncertainties on the rotation rates.

The purpose of this paper is to present the use of the Lomb-Scargle Periodogram

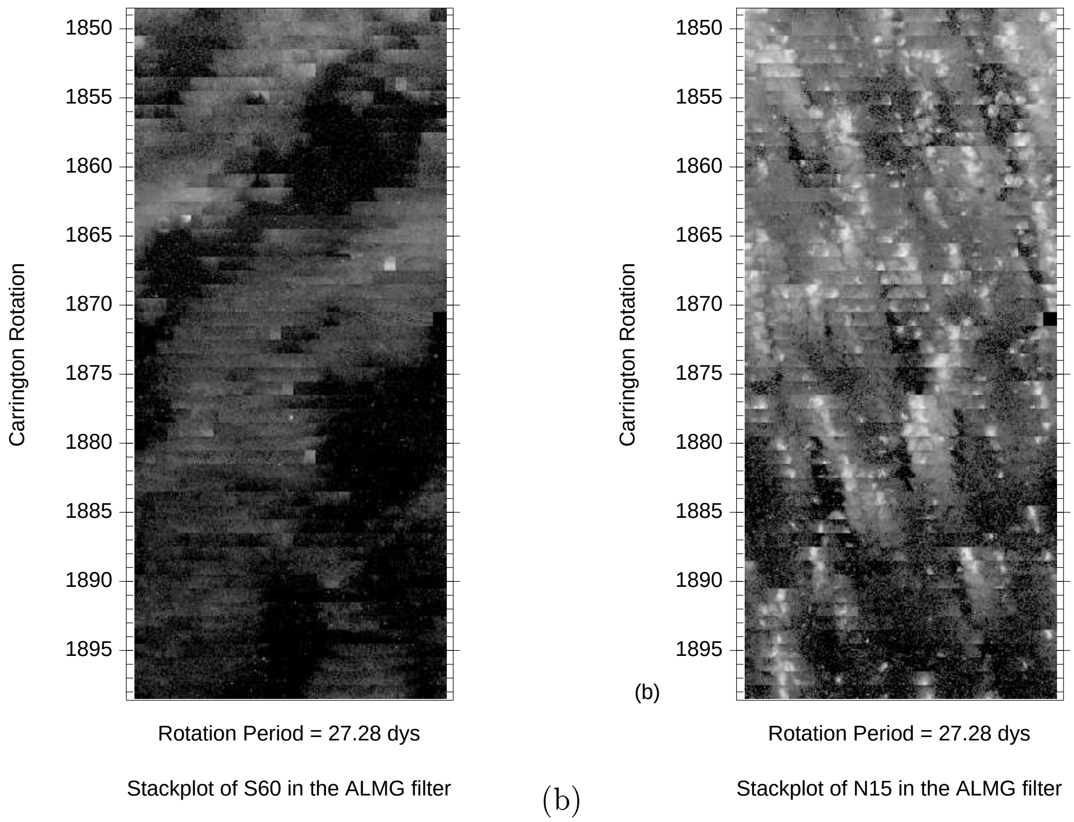

(a) (b)

Figure 2.1: *(a)* A Carrington stackplot of 60° S, well outside the activity belt, as seen by *Yohkoh*/SXT. The timespan is from November 1991 to August 1995. The largest features persist for well over a year, and smaller features can be seen to evolve. The slopes of features moving down the plot indicate their individual rotation rate relative to the Carrington period of 27.3 days. *(b)* A similar stackplot for 15° N, positioned over the most active latitudes. The tracers slope in the opposite sense from (a), indicating that they are moving faster than the Carrington rate. Note how different features can be simultaneously moving at different rates. The presence of strong parallel features will produce harmonics of the rotation frequency in the periodogram analysis.

in a method which addresses two weaknesses of the autocorrelative approach: identification of simultaneous rotation rates, and discrimination between the variance among these tracer rates and short-term "noise" which contributes to the uncertainty in the measurements. A separate analysis of the data by autocorrelation demonstrates that the two methods give consistent results for the mean rotation rate as a function of latitude. The groundwork is laid in Section 2.2 with a brief discussion of the dataset and reduction methods used to produce the time-series. Section 2.3 describes the principal analysis method of the paper and presents results. The data are re-analyzed in Section 2.4 by autocorrelation for comparison and checking with the results of the spectral analysis. Also, autocorrelation provides a measure of tracer lifetimes which is consistent with the assumptions of this study. Section 2.5 contains some further discussion of salient points.

2.2 Data Reduction

The datasets are derived from processed *Yohkoh*/SXT images, called "SFD images". The SFD images are composed of a long and short-exposure pair of images to provide a dynamic range of 1×10^6 (in instrument units DN). The pair of exposures are taken with the same diagnostic filter, are corrected for background and saturation, and are normalized in time and resolution (Morrison 1994). This study spans the six years 1992–1998; after removing corrupted images, the mean sampling rate for the SFDs was approximately 20 per day for the Al.1 diagnostic filter, and 40 per day for the

AlMg filter. The six-year datasets are separated into one-year segments which start on the beginning of each calendar year. Datasets of one-year length were chosen to mitigate seasonal variations of the Earth's velocity about the Sun. Modulations of the data due to the Earth's distance from the Sun and the tilt of the solar axis are addressed by the method of data reduction as described below. This length (of one year) encompasses several cycles of the frequencies under consideration, while remaining comparable in scale to the tracer lifetimes (as shall be demonstrated in Section 2.4.3).

To study the latitudinal variation of the solar rotation, time-series are analyzed for different latitude regions. These latitude zones are defined by boundaries along heliocentric latitude and longitude lines in each image. Each zone spans one degree in the longitudinal direction and is centered on the central meridian. Each zone spans fifteen degrees in the latitudinal direction, and they are centered every 15 deg from 60° S to 60° N, giving a total of 9 zones. The proportions of the zones were chosen to provide high resolution in the longitudinal direction (along which the solar rotation is measured), while maintaining a sufficient number of pixels in each zone to provide a statistically meaningful estimate of the mean SXR emission. The longitudinal span of one degree is also the approximate angular rotation of the Sun during one orbit of the *Yohkoh* spacecraft (~ 97 min), which is about half of the sampling rate for the SFD images in either diagnostic filter. (The logic of this arrangement is discussed further in Section 3.2.) The location of the set of zones was chosen to minimize projection effects.

The image data are reduced to a time-series[2] for each latitude bin Θ and year Υ: $\mathcal{Y}(\Theta, \Upsilon)$. An element of a time-series ($y_i = y(t_i)$) is calculated using the spatial average of the SXT signal over the zone's pixels, at image time t_i. This spatial averaging corrects for variations of the apparent shapes and sizes of the zones due to the annual cycling of the solar B0-angle and Sun-Earth distance.

Frequency analysis is performed on the *natural logarithm* of the data:

$$\mathcal{Z}(\Theta, \Upsilon) \equiv \ln \mathcal{Y}(\Theta, \Upsilon). \tag{2.1}$$

While the time-series $\mathcal{Y}$ could be analyzed directly for rotation signals, it is worth considering that the SFD images have a dynamic range of six orders of magnitude, and only the bright cores of active regions access the upper three orders for extended periods of time (e.g., over a solar rotation). At such a scaling, the time-series are dominated by brightness spikes which correspond to active region centers. Although the solar rotation can be seen as a general modulation of the SXR "background", the spectral content of the active latitudes is greatly affected by these impulsive features. Such effects include convolutions of the spectra with high frequencies (i.e., "ringing"), and even suppression of peaks. Figure 2.2 uses periodograms to illustrate these effects on the data in the frequency domain. (A periodogram is an estimate of a function's

[2] The SFD database is composed of images, each taken with one of two diagnostic filters. Data taken with two different filters cannot be related in a simple way, so instead the database was partitioned into two concurrent sets, analyzed separately, and the final results averaged together. For the sake of simplicity, and since the two data sets were treated identically, the "filter label" is not made explicit in the description of the analysis procedures.

power spectral density, or PSD. This is analogous to the set of $|c(\omega)|^2$, where $c(\omega)$ are the Fourier coefficients of an evenly-sampled function. The particular type of periodogram used in this paper is described more fully in Section 2.3.1.)

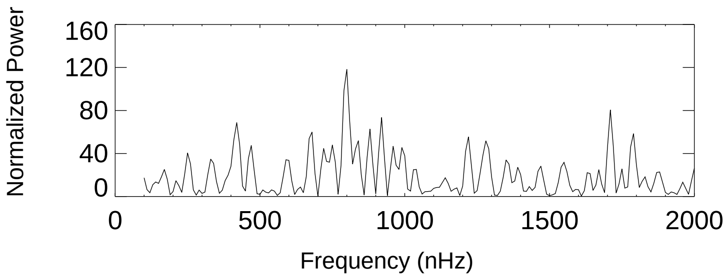

(a)

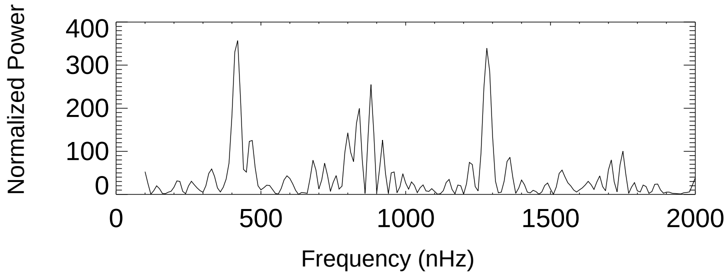

(b)

Figure 2.2: *(a)* The periodogram of an uncompressed time-series (latitude 15° N, year 1992), calculated in the neighborhood of the rotation fundamental ($\approx$ 410 nHz) and first two harmonics. Carrington rotations 1851–1864 of Figure 2.1(b) correspond to this time-series. *(b)* Periodogram of the same time-series after the data has been logarithmically compressed. Note the suppression of "ringing" and the emergence of two more significant peaks. (The frequencies of these peaks can be identified with tracer slopes in the stackplot, and so can be argued to have physical relevance.) Note: the power scaling should not be compared between (a) and (b), since they are normalized differently.

However, the corona is composed of structures of widely differing sizes, magnetic strengths and connectivities, and differing plasma densities and temperatures, and active region cores represent only one (albeit an important) component. Images of the SXR corona, as illustrated with data from SXT and similar instruments, are typically displayed on a logarithmically-compressed scale (of integrated photon energy in the case of the SXT, viz., Tsuneta et al. (1991)), and reveal many of the coronal features described in the phenomenology. As the apparent rotation rate of the soft X-ray corona is a function of the (possibly variant) rotation rates of these features, which in turn reflect the features' boundary locations, it is useful to de-emphasize the power of active region cores in the uncompressed data relative to the contribution of other types of features. A logarithmic scaling emphasizes the "background rotation modulation" mentioned above. For latitudes close to the equator where active regions are present, the log-compressed time-series are much less impulsive in character, and more sinusoidal, than the non-compressed versions. In the case of latitudes poleward of the activity belt, where active regions are absent, analyses of the compressed and uncompressed data do not give significantly different results.

2.3 Spectral Analysis

This section describes the principal method used to analyze the time-series data for rotation signals. The Lomb-Scargle periodogram gives an estimate of the power spectrum of a time-series, such as can be produced by traditional Fourier analysis. Before going into more detail on the method of data analysis, a brief introduction to the Lomb-Scargle periodogram is given.

2.3.1 The Lomb-Scargle periodogram

The power spectra were produced using the Lomb-Scargle periodogram (LSP) (viz. Scargle 1982; Horne & Baliunas 1986). For the time-series $\mathcal{Z}$, with N_0 number of elements $z_i \equiv z(t_i)$, Scargle (1982) defines the normalized periodogram as a function of frequency as

$$P_{\mathcal{Z}}(\omega) = \frac{1}{2\sigma_{\mathcal{Z}}^2}\left\{\frac{\left[\sum_{j=1}^{N_0}(z(t_j)-\bar{z})\cos\omega(t_j-\tau)\right]^2}{\sum_{j=1}^{N_0}\cos^2\omega(t_j-\tau)}+\right.$$
$$\left.+\frac{\left[\sum_{j=1}^{N_0}(z(t_j)-\bar{z})\sin\omega(t_j-\tau)\right]^2}{\sum_{j=1}^{N_0}\sin^2\omega(t_j-\tau)}\right\}, \qquad (2.2)$$

where τ is defined by the equation

$$\tan(2\omega\tau) = \left(\sum_{j=1}^{N_0}\sin 2\omega t_j\right) \Bigg/ \left(\sum_{j=1}^{N_0}\cos 2\omega t_j\right). \qquad (2.3)$$

and

$$\bar{z} \equiv \frac{1}{N_0}\sum_{j=1}^{N_0} z_j, \qquad (2.4)$$

$$\sigma_{\mathcal{Z}}^2 \equiv \frac{1}{N_0-1}\sum_{j=1}^{N_0}(z_j-\bar{z})^2. \qquad (2.5)$$

The advantages of this approach over the conventional discrete FFT are that the LSP is designed to handle unevenly sampled data without bias and that the height of the most significant peak in the frequency domain gives a measure of the "false-alarm probability", i.e., the statistical chance that the peak is due to Gaussian noise.

Fundamentally, the LSP performs a linear least-squares fit of a sinusoid of the given frequency,

$$z(t) = A_\omega \sin(\omega t - \phi_\omega), \tag{2.6}$$

to the time-series data (Press et al. 1992). Hence, the periodogram can easily be used to select filtered signals *à la* Equation (2). The spectra were investigated over a frequency range that encompassed reasonable values for the rotation frequency and its first five harmonics.

2.3.2 Method

To determine the solar rotation (and its spread across time and tracers), an iterative scheme is used to filter out the most significant sinusoidal fits to the data. More precisely, the periodogram is first calculated across the entire range, and then recalculated at a finer frequency resolution in the neighborhood of the highest peak. The most significant frequency, ω_k, determined by the highest peak in the periodogram, is used to perform a linear least-squares fit to the data with a sinusoid of the form

$$\psi_k(t) = A_k \sin(\omega_k t - \phi_k). \tag{2.7}$$

This signal is subtracted from the data in the time-domain. A new periodogram is then calculated and searched for the new most-significant peak, etc. In essence, the data are partially decomposed into a limited set of sine waves, according to the form of Equation (7), where $k = 1, 2, \ldots, K$.

The decomposition iteration is continued until all signals of amplitude A_k such that

$$A_k \geq \frac{1}{10}\sigma_{\mathcal{Z}} \tag{2.8}$$

are found, where $\sigma_{\mathcal{Z}}$ is the total statistical deviation of the time-series data. Of these, only frequencies which fall between 370 and 470 nHz (synodic periods $31^{\mathrm{d}}.3$ and $24^{\mathrm{d}}.6$, respectively), or within the respective frequency ranges in the case of rotation harmonics, are retained. (It was straightforward to identify higher frequency signals with particular rotation harmonics. The presence of higher longitudinal wavenumbers was verified by referring to the corresponding stackplots.) The boundaries of 370 and 470 nHz were chosen arbitrarily to embrace the frequency range within which one might reasonably expect to observe the rotation signals of persistent tracers. The sensitivity of the results upon the choice of boundary values was not investigated quantitatively; however, a casual survey of the data suggests that the majority of the extracted signals were located comfortably within these limits.

The weighted (by the signal-to-noise ratio) mean and deviation of this subset of frequencies are taken as the mean rotation frequency and spread for that latitude and time period, for that diagnostic filter. The final results for the two filters are then combined.

2.3.3 Frequency determination and uncertainties

The harmonic content of the time-series $\mathcal{Z}(\Theta, \Upsilon)$ may be presumed composed of harmonic signals of various (and varying) amplitudes, phases, and durations, which are formed by the repeated passage of persistent features across the field of observation. An attempt to derive a single characteristic rotation rate would presumably use some weighted combination of these signals (if they were known). Insofar as these "real" signals differ from pure sinusoids of one-year length, spectral analysis will not be able to provide a finite one-to-one set of signal solutions, but it is assumed that a finite set of sinusoids which represents a sufficient amount of the harmonic content of the data will have a (weighted) mean and deviation which are sufficiently close to that of the distribution of the "real" signals, so this mean can be used as the characteristic rotation rate, and the deviation can be used to characterize the "real" variations in tracer signals.

The basis for this set of assumptions lies in the distinction of perturbations as presented in the Introduction, to wit, perturbations on the timescale of tracer lifetimes (slow), and perturbations on the timescale of the sampling rate (fast). A perfectly constant tracer signal could ideally be fit with a single sinusoid of equal power. Changes in a tracer signal which are gradual compared to the lifetime and the length of the time-series will cause the corresponding spectral peak to leak some of its power to sidelobes. It would require more than one sinusoid to fit the same amount of power as in the ideal case, and the total power of the sinusoidal fits will have a distribution that is maximally (by least-squares estimation) close to the power distribution of the tracer signal.

Following this reasoning, the characteristic rotation frequency $\omega(\Theta, \Upsilon)$ for the time-series $\mathcal{Z}(\Theta, \Upsilon)$ for latitude Θ and calendar year Υ is defined as

$$\omega(\Theta, \Upsilon) \equiv \frac{\sum_{k=1}^{K} \xi_k \omega_k}{\sum_{k=1}^{K} \xi_k}, \tag{2.9}$$

where the ω_k correspond to those frequencies iteratively derived from the LSP which lay within the expected synodic fundamental frequency range of 370 to 470 nHz, or harmonics[3], as used in Equation (2). The signal-to-noise ratio

$$\xi_k \equiv \frac{A_k^2}{\sigma_n^2} \tag{2.10}$$

is used as the weight, where

$$\sigma_n^2 \equiv \frac{\sum_{j=1}^{N_0} [z(t_j) - \bar{z} - \sum_{k=1}^{K} \psi_k(t_j)]^2}{N_0 - 1} \tag{2.11}$$

is the variance of the data after removal of the sinusoidal fits. As discussed above, the variance *within the set of* ω_k is taken to represent a physical variance among tracer rotation rates, and hence describe a gamut of "real" rotation rates on the Sun. This

[3]Harmonic signals of the fundamental rotation frequency were included in these calculations by dividing their frequency by their order.

is defined by the weighted variance

$$s^2(\Theta, \Upsilon) \equiv \frac{\sum_{k=1}^{K} \xi_k (\omega_k - \omega)^2}{\sum_{k=1}^{K} \xi_k - \bar{\xi}}. \tag{2.12}$$

Next we estimate the precision of the frequencies determined from the LSP analysis. First, the "fast" noise in the time-series data is used to put uncertainty limits $\pm\Delta z_i$ on the data z_i. The *Yohkoh* satellite has a 97-min orbit and collects data during about 60 min of that period. The latitude bins are one degree wide, which is approximately the rotation distance of the Sun over one *Yohkoh* orbit. Hence, the variance of the time-series data $\mathcal{Z}(\Theta, \Upsilon)$ among datapoints from the same orbit are caused by transient SXR brightenings and non-uniformity of the SXR corona over spatial scales of 1° (heliocentric), and represent a real uncertainty in the measuring process. The sampling rate is approximately twice per orbit, for each of the two diagnostic filters. For calculation of this error estimate, the data are binned by spacecraft orbit number. For those orbits i having two or more data points, a statistical deviation is calculated and the value assigned to Δz_i. The set of Δz_i for each time-series was found to have a very robust median value, so this median was adopted as a constant value for the respective time-series. Now, the resolution in frequency discrimination can be defined as follows. Over the course of a tracer lifetime, two simultaneous signals ω_1 and ω_2 are considered to be critically resolved if one signal lies within $z_i \pm \Delta z_i$ at all times t_i and the other signal only lies within $z_i \pm \Delta z_i$ for half of the times t_i. Assuming a tracer *total* lifetime of 6 rotations (which is consistent with Figure 2.1), all time-series

Table 2.1:

SXR coronal synodic rotation periods (±0.7 days) : spectral analysis

Year	Latitude Bin								
	$-60°$	$-45°$	$-30°$	$-15°$	$0°$	$15°$	$30°$	$45°$	$60°$
1992	28.1	27.8	28.0	27.4	27.2	27.2	27.5	28.0	28.1
1993	28.2	27.2	27.3	27.5	27.4	27.6	27.5	27.4	27.8
1994	27.7	27.4	27.3	27.1	27.1	27.4	27.4	27.3	27.8
1995	27.9	27.5	27.2	27.1	26.9	27.0	26.9	27.0	27.4
1996	28.2	28.0	27.4	27.4	27.2	26.8	27.3	27.7	28.0
1997	28.5	28.9	28.3	27.2	27.2	27.3	27.8	28.6	28.8

give a relative uncertainty of $\frac{\Delta\omega}{\omega} \approx 0.025$, or, for a reasonable example of a synodic frequency, $\omega = 410 \pm 10$ nHz.

2.3.4 Results

In this section, the method of partial decomposition described heretofore is applied to the data to characterize the rotation of the SXR corona during the declining phase of the last solar activity cycle, i.e., the years 1992–1997. The mean profile is compared to other layers of the atmosphere to demonstrate two general features of the coronal rotation: (1) the latitudinal gradient is comparatively shallow, and (2) the rigid rate is approximately equal to the equatorial rate for sunspot groups. The questions of north-south asymmetry and rigidity can be respectively quantified by fits to a line and to the traditional form $\omega = a - b\sin^2\theta - c\sin^4\theta$. Additionally, the decomposed set of signals $\psi_k(t)$ facilitates quantitative measure of the variance among tracer rates.

The analysis method provides a single rotation frequency per latitude bin, per year segment, per diagnostic filter. Since the time-series associated with the filters are effectively simultaneous and independent, the final frequencies were calculated as averages between the two filter values. Table 2.1 lists the periods corresponding to these synodic rotation frequencies, which have been derived using all of the significant components of the fundamental rotation and the first four harmonics, weighted by the signal-to-noise ratios, according to Equation (2.9). For the sake of clarity, plots of all of the rotation profile curves are not included here, but the details of the latitudinal and temporal variations can be discerned in Table 2.1. (Note that the 2.5% relative uncertainty derived in the previous section becomes about a $0^{\mathrm{d}}.7$ absolute uncertainty for these values.) For all years, the rotation rates of the active latitudes (between 30° S and 30° N) appear rigid, although they also lie within about 1σ of the sunspot group rates as determined by Howard (1984), so the question of rigid rotation *within* the activity belt is not clearly resolved within the uncertainties.

This behavior is evident in Figure 2.3, which averages the rotation rates across the yearly parameter to produce a single rotation curve for the entire time period, which covers roughly the descending phase of the last activity cycle. Curves for sunspot groups, the K-corona, and the photosphere are overplotted for comparison and context, although one is cautioned that these other studies were done during different cycles, for different phases and coverage of the 11-year activity cycle. This caveat might explain the surprising apparent discovery that the SXR corona rotates faster than the K-corona at high latitudes. (This is revisited in Section 2.5.) The error bars indicate the precision of the frequency estimates, as defined in the previous section. There is a strong suggestion that the corona rotates rigidly, with the higher

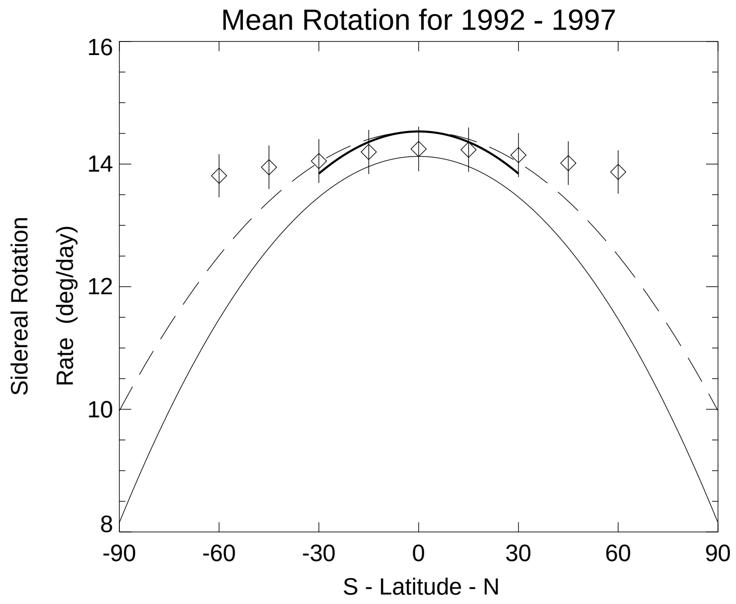

Figure 2.3: The rotation profile across latitude for all years averaged. The error bars indicate the uncertainty. *Short solid line*: sunspot groups; *thin solid line*: Mt. Wilson Doppler measurements of the photosphere; and *dashed line*: the white-light K-corona. This figure borrows heavily from Figure 9 of Howard (1984).

latitudes moving faster than other layers of the atmosphere.

The rigidity of the latitudinal profile is best described by a polynomial fit to the symmetric component of the data. Table 2.2 includes the coefficients $\{a, b, c\}$ corresponding to the traditional model for describing solar differential rotation. The b term is negligible in all cases, so the c term is considered for the amount of differential rotation. According to these fits, the difference between rotation rates at the equator and the highest measured latitudes (60°) are at about 1–2σ of the estimated uncertainty in the values. This implies that any differential rotation is very small, but measurable.

The asymmetric (about the equator) component of the data is most simply fitted

Table 2.2:

Curve fits to sidereal rotation rates

Year	$\omega = n + m\theta$ (deg per day)		$\omega = a - b\sin^2\theta - c\sin^4\theta$ (deg per day)		
	n	m	a	b	c
1992	14.0	0.0003	14.1	-1×10^{-6}	0.6
1993	14.1	0.0006	14.2	-6×10^{-8}	0.4
1994	14.1	-0.0003	14.2	5×10^{-7}	0.4
1995	14.2	0.002	14.3	-5×10^{-8}	0.5
1996	14.1	0.001	14.2	1×10^{-6}	0.8
1997	13.8	0.0004	14.0	1×10^{-6}	1.0
Mean	14.1	0.0008	14.2	5×10^{-7}	0.7

by a line, and Table 2.2 contains these coefficients, too. The slopes m are too small in comparison to the estimated uncertainties to suggest or confirm any north-south asymmetries in the rotation rate for time periods of a year or longer.

The coefficients in Table 2.2 suggest that the differential gradient (term c) increased, and the coronal rotation rate (terms n and a) decreased, with the rise of the new activity cycle, but at only a 1σ level of certainty. Reference to Table 2.1 indicates that the most poleward latitudes exhibited the largest variance in rotation rates (2σ certainty), while the temporal behavior of latitudes within the activity belt is not clearly determined within the estimated limits of uncertainty. Figure 2.4 explores further, comparing years 1994 (bottom of solar activity cycle) and 1997 (start of new cycle). Specifically, the latitude bins nearest the emerging flux of the new activity cycle are most greatly affected, approaching the projected curve for sunspot groups. This effect is for the overall rotation profile to reduce its mean rotation rate, and to become more differential.

(a) 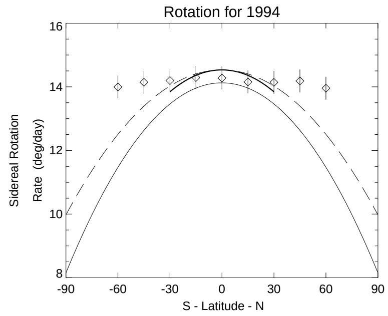

(b) 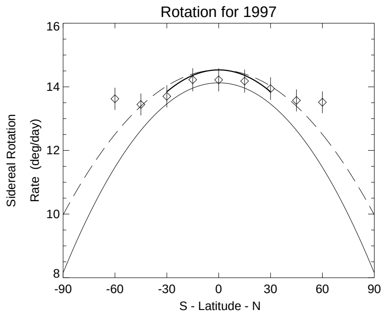

Figure 2.4: *(a)* Differential rotation plot for nadir of the activity cycle. Note the flat profile of the data, and that the rotation rates for the 45° bins are faster than the other curves at those latitudes. *(b)* Similar plot for rise of the activity cycle. The 45° bins show the biggest change, causing the rotation profile of the data to be more differential. (See Figure 2.3 for key.)

Not only can the mean rotation rate of a latitude bin change from year to year, it is an argument of this paper that there can be multiple tracer rotation rates at each latitude during the year. The variance s^2 (see Equation (2.12)) provides a measure of the spread in rotation values. The calculated $s^2(\Theta, \Upsilon)$ show no strong dependence upon either latitude Θ or year Υ. For all latitudes and years, the deviation $\sqrt{s^2}$ of the tracer rates about their mean is approximately 1–2σ uncertainty levels. In terms of the partial spectral decomposition method, this implies that the power in the vicinity of the solar rotation frequency (and its harmonics) is more widely distributed in a few significant components than the resolution of uncertainty estimation. In terms of SXR tracers, this is interpreted as a spread in rotation rates which is measurable at the bounds of certainty in this study.

2.4 Autocorrelation

The technique of autocorrelation has often been applied in previous studies of coronal rotation: Parker, Hansen, & Hansen (1982), and Sime, Fisher, & Altrock (1989), for example. This approach to period estimation avoids some of the problems of direct Fourier analysis (like aliasing), while permitting a straightforward identification of any dominant signal. Furthermore, Fisher & Sime (1984) demonstrated how the diminution of the rotation peak at advanced lags due to the evolution of coronal tracers can be described as an exponential decay, thus providing a measure of tracer lifetimes. The method of harmonic filtering, as described in the previous section, is useful for analyzing a spread of intermixed rotation rates in a quantitative fashion, so the two methods may be used in a complementary fashion to describe the evolution of coronal SXR tracers. Also, period estimations can be compared to compare results. (It should be noted that autocorrelation is akin to Fourier analysis—the cosine transform of the autocorrelation function gives the Fourier power spectrum—and the Lomb-Scargle Periodogram is essentially a least-squares fit of sinusoids, so discrepancies in the results contain information about how well these methods represent the harmonic content of the data.)

2.4.1 Data correlation

The autocorrelation procedure requires that the data be evenly sampled. To accomplish this, the log-compressed time-series data were binned by spacecraft orbit (a period of approximately 97 minutes) and averaged; interpolation filled the data gaps. ($\mathcal{Z}(\Theta, \Upsilon) \rightarrow \mathcal{Z}'(\Theta, \Upsilon)$, and $z(t_i) \rightarrow z'(t'_b)$, where $b = 1, 2, \ldots, B_0$.) The autocorrelation function $\rho_{\mathcal{Z}'}(L)$ of the time-series $\mathcal{Z}'$ as a function of the lag L is

$$\rho_{\mathcal{Z}'}(L) = \frac{\sum_{b=1}^{B-L}(z'_b - \bar{z'})(z'_{b+L} - \bar{z'})}{\sum_{b=1}^{B-L}(z'_b - \bar{z'})^2}. \tag{2.13}$$

The most significant positive peak in the range of $24^{\mathrm{d}}.6$ to $31^{\mathrm{d}}.3$ was identified, and the center-of-mass calculated as the period estimate. Finally, the results were averaged between filters.

2.4.2 Results

The SXR differential rotation, as calculated by autocorrelation, agrees qualitatively with previous investigations of the corona, and agrees quantitatively with the results of the spectral analysis presented in Section 2.3. The values in Table 2.3 are within the uncertainty (± 0.7 days) of the corresponding entries in Table 2.1, with only a couple of exceptions.

2.4.3 Correlation timescales

A fundamental assumption of this study is that the SXR rotation modulation is produced by the repeated passage of persistent features, and that the timescale for this persistence is on the order of several months. Evidence to support this has been presented in Figure 2.1, which shows stackplots of SXR synoptic data for two

Table 2.3:

SXR coronal synodic rotation periods : autocorrelation

Year	Latitude Bin								
	-60°	-45°	-30°	-15°	0°	15°	30°	45°	60°
1992	27.8	27.8	27.8	27.7	27.6	27.5	27.7	27.8	27.8
1993	27.8	27.7	27.7	27.6	27.4	27.5	27.6	27.8	27.8
1994	27.5	27.5	27.5	27.3	27.3	27.3	27.5	27.5	27.5
1995	27.8	27.6	27.6	27.5	27.1	27.4	27.6	27.7	27.7
1996	28.3	28.2	28.2	27.9	27.8	27.8	28.1	28.4	28.3
1997	28.6	28.6	28.4	28.2	28.0	28.2	28.5	28.6	28.5

distinct regions. Since each strip of the stackplot represents approximately 27 days, these figures convincingly demonstrate the persistence (downward streaking) of some coherent elements of the corona for months or longer.

A more quantitative estimate of structure lifetimes using the autocorrelation function was introduced by Fisher & Sime (1984) in their study of the rotational properties of the K-corona, and has also been used to good effect by Sime, Fisher, & Altrock (1989) in their study of coronal rotation using the Fe XIV emission-line. They define the timescale τ_c by

$$\tau_c = -\frac{P_{corona}}{\ln \rho(P_{corona})}, \tag{2.14}$$

where P_{corona} is the lag of the rotation period. The parameter τ_c is simply the timescale for exponential de-correlation of the data at the rotation period, i.e., over time τ_c the probability of seeing a repeat passage of the tracer around the Sun drops by $1/e$.

Figure 2.5 displays the timescales for the six-year period of the study. Also in-

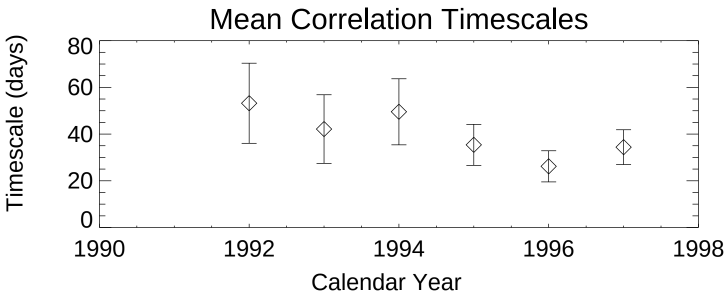

Figure 2.5: Timescales for exponential decorrelation of SXR features. The datum per year is an average over all latitude bins. The error bars indicate a standard deviation in timescale for the latitude bins in that year.

dicated is the span in timescale values over the latitude bins. During the declining phase of the activity cycle there appears to be a trend towards shorter tracer lifetimes, and the range of lifetimes decreases as well. The time for one e-folding is between one to two rotations, which is comparable to the results found by Fisher & Sime (1984) for the green-line corona. As in their study, the results imply tracer lifetimes longer than one solar rotation, at a minimum, and as long as two in some cases, further validating the assumption of persistent tracers.

2.5 Discussion

In contrast to calculating the rotation frequency directly from the centroid of a peak in the autocorrelation function (which considers *all* of the power in the selected frequency range, due to both noise and signals), the approach developed in this study only gives weight to the power of a finite set of the most significant signals which demonstrably approximate the actual data. This method also provides a natural (if somewhat arbitrary) distinction between the uncertainty due to noise and the uncertainty due to a "real" spread in the values of tracer rotation rates during the year. Simply, the deviation amongst the most significant fitted signals represents the physical spread of the solar rotation rate, and the deviation of the data after removal of these signals, σ_n, is considered to be the deviation of the noise.

The set of isolated signals can be combined to estimate a mean rotation frequency of the time-series data, weighted by the signal-to-noise ratio. Results of studying the corona with *Yohkoh*/SXT data indicate that the SXR corona shows some of the same qualitative rotational behavior as discerned in other studies, such as those of the white-light corona by Hansen, Hansen, & Loomis (1969) and Fisher & Sime (1984). In particular, near the equator the corona rotates at a speed close to that of the photosphere. (The uncertainty levels do not permit identification with sunspot or Doppler rates exclusively.) The differential profile with latitude is almost rigid throughout the period of the study; however, uncertainties are small enough to measure the amount of differential rotation, which would allow a lower bound to be placed on the differential rotation measure. The mean rotation rates and differential measure are observed to change over the course of the study. The deceleration of the corona to photospheric rates at the latitudes of new-cycle emerging flux is suggestive of the possibility that (1) this observed evolution is tied to the solar activity cycle, and (2) the corona can be broadly affected by localized flux concentrations. This suggestion is made by observing that the increased incidence of concentrated flux corresponds to the emergence of new-cycle active regions, which produce a rise in the overall SXR emission at that latitude and strongly contribute to the observed rotation modulation. The rotation rate of active region tracers is expected to follow the photosphere more closely than those of large-scale, diffuse regions (Wang et al. 1988). Nevertheless, this study is of insufficient length (six years) to tie any firm conclusions to the activity cycle.

Not only does the mean rotation rate at the latitude of activity (and equatorwards of there) tend to adhere closely to the photospheric profile, but it is also observed that the latitudes poleward of this latitude tend to show a more rigid profile. (Refer back to Figure 2.4.) Since the SXR corona is optically thin, an instrument's line of sight passes through a large volume of the solar atmosphere. Hence, projection effects on the solar disk around large structures, like active regions, can be significant at higher latitudes. The projection of tracer structures across higher latitudes could influence the differential rotation profile to appear more rigid in that region. In principle, the contribution of projection effects across latitude bins could be investigated by cross-correlating (between latitude bins) sets of significant components. Tracer structures which project across two latitude bins should produce similar components in each latitude's spectrum. Since the LSP is equivalent to linear least-square fitting of sinusoids to the data (see Section 2.3.1), components can be compared in amplitude, frequency, and most importantly, phase.

The differential rotation curves included from other studies are intended to provide some context to the Figures in which they appear, but may not be suitable for strict comparison. It bears repeating that these studies were done for differing coverages of different activity cycles. As an example, it is provocative to note that the SXR profile is more rigid, and hence faster at higher latitudes, than the K-corona curve. The opposite situation is perhaps expected, as the SXR emission mostly comes from altitudes lower than those observed in the study by Hansen, Hansen, & Loomis (1969). The apparent inconsistency between results and expectations is perhaps due to a discrepancy in rotation rates from different activity epochs. Furthermore, broadband SXR emission is affected by both plasma temperatures and emission measures, whereas white-light observations are dominated solely by electron density. The convolution of heating centers with density structures in the corona may show up different features in X-rays than in white-light.

The spread in spectral components of the rotation "band" is equal to, and sometimes moderately larger than, the frequency resolution imposed by the uncertainty estimates. This quantifies an observation which can be made by visual inspection of stackplots, such as those in Figure 2.1: the SXR corona can evince multiple rotation frequencies simultaneously, in the same latitude bin. As a consequence, one expects that the concept of a "mean rotation rate per latitude bin" breaks down at the level where relative uncertainties on the frequencies reach $1 \sim 2\%$. More sophisticated studies of coronal rotation rates will need to take multiple signals into account, or re-examine operational definitions of the rotation rate, insofar as the data from this six-year study is representative of the general behavior of the corona.

CHAPTER 3

BIMODAL BEHAVIOR IN SOLAR ROTATION RATES

3.1 Introduction

It has been observed that the rotation of the solar atmosphere varies greatly among types of features. In particular, many large-scale magnetic patterns appear to rotate more slowly than the local photospheric plasma in which they appear, and have a more "rigid" profile versus latitude than smaller features or the Doppler-measured photospheric plasma. Although coronal holes are the most commonly cited example of this phenomenon (e.g., Timothy, Krieger, & Vaiana 1975), the unipolar distributions of magnetic flux at the photosphere in which the coronal holes are rooted can also display this behavior, especially at latitudes away from the activity belt.

Sheeley, Nash and Wang (hereafter SNW) have done extensive work (Sheeley, Nash, & Wang 1987; Wang et al. 1988; Nash, Sheeley, & Wang 1988; Wang, Nash, & Sheeley 1989; and Wang & Sheeley 1993) demonstrating that this behavior can be explained purely by surface flows (e.g., differential shear, meridional flows), and the eruption and diffusion of concentrated magnetic flux. Their work is based on previous flux-transport models (e.g., Leighton 1964 and Devore, Sheeley, & Boris 1984). They point out that it is unnecessary to invoke hidden motions of structures or layers beneath the photosphere.

The rotation rates of coronal features can be followed in the solar soft x-ray emission, such as is measured by the *Yohkoh* Soft X-ray Telescope (Tsuneta et al. 1991). This paper introduces the observation that during the declining phase of solar cycle 22, the south polar coronal hole extension exhibited two separate "phases". These phases were characterized by shape, rotation velocity, and relatively abrupt transitions. The behavior of the coronal holes reflected that of the underlying unipolar magnetic patterns, which in turn evolved in a manner consistent with the SNW model. This paper also demonstrates that the observed bimodal behavior can be adequately described by the (observed) emergence of concentrated flux through the photosphere and its subsequent transport across the surface. It is argued that one phase corresponds to the "random" emergence of flux across longitude (and about the activity belt), and the other phase is produced by the presence of an active longitude at which flux is repeatedly introduced to the photosphere over several rotations.

3.2 Observation of Bimodal Behavior

The Soft X-ray Telescope (SXT) onboard the Japanese satellite *Yohkoh* records the broadband thermal emission of the solar corona above about 2 MK. Coronal holes, being lower in plasma density and temperature than the typical "quiet corona", appear as regions of little or no signal. During the years 1991–1994 the sun entered the declining phase of solar cycle 22 but the overall SXR brightness of the sun was still high enough that coronal holes appeared in contrast. Stackplots of SXT data at high latitudes clearly indicate the presence and local behavior of the polar coronal hole extensions (c.f., Figure 3.1 and Weber et al. 2000).

As time advances down the stackplot, it appears that the coronal hole alternated between two behaviors, or phases. In one case the hole appears to have a slow rate of rotation (as indicated by its slope on the stackplot), be relatively narrow in longitude, and weak in the sense that the extent of the region is poorly defined due to the registration of some SXT signal. This is labelled the "slow (S) phase". In the other case, labelled the "fast (F) phase", the hole recurs at the faster Carrington rate (as indicated by a vertical slope on the stackplot), is wider ($\sim 150°$ in longitude), and is well-defined in its extent. Furthermore, the transition between these phases is relatively abrupt (1–2 rotations) versus the lifetime of the phases ($\sim$ 6–10 rotations).

Not surprisingly, a comparison with Kitt Peak magnetograms for the same period shows that the locations and shapes of the coronal holes follow those of the weak unipolar magnetic regions of the photosphere in which they are rooted. It should be noted, however, that the boundary of a coronal hole lies some distance within that of the encompassing unipolar region which is necessarily circumscribed by a polarity inversion line. Coronal holes correspond to regions of open field lines, and the maintenance of a coronal hole boundary at a polarity inversion line would imply a large surface discontinuity in the magnetic field and Ampere's Law would require

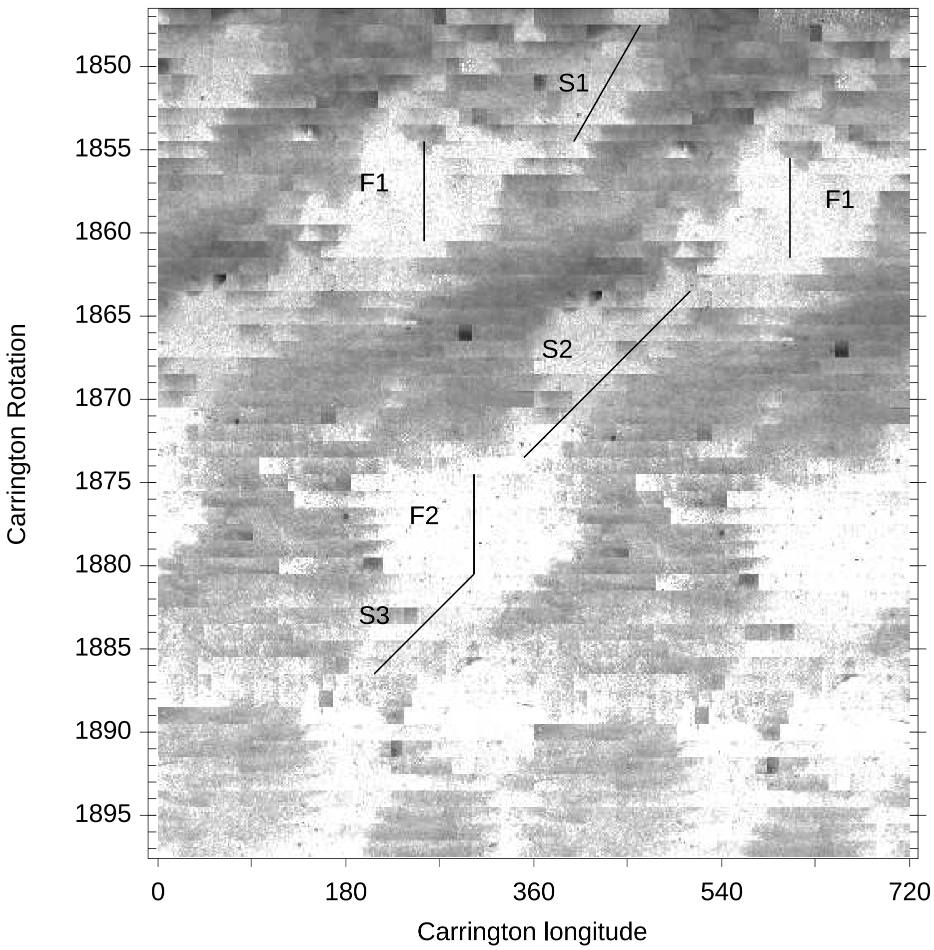

Figure 3.1: A Carrington stackplot of 60° S, well outside the activity belt, as seen by *Yohkoh*/SXT. The timespan is from November 1991 to August 1995. High soft x-ray signal is shown in black; the south polar coronal hole extension appears as a low signal (in white). The stackplot has a width of 720° so features appear doubled in the horizontal direction. The solid lines indicate the approximate center and stackplot slope (i.e., rotation rate) of the coronal hole region at different times. The alternation between the (S) and (F) modes is clear.

improbably large and steady current-sheets in the corona.

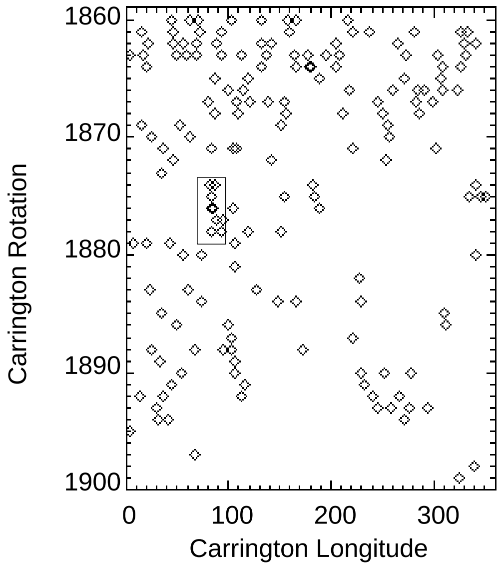

Figure 3.2: This plot shows the longitudinal coordinate of large bipoles of concentrated flux in the southern solar hemisphere, as observed in Kitt Peak magnetograms. The latitudinal coordinate is suppressed. The sustained infusion of flux at $\sim 85°$ longitude during rotations 1874–1878 is the feature of note here. Also notice the lack of new flux immediately eastward of this region.

Figure 3.2 shows the longitudes of flux concentrated in bipoles in the southern hemisphere over several rotations. (The latitudes are suppressed.) This data was gathered by identifying groups of contiguous pixels with values $\geq 800\,\mathrm{G}$ in the Kitt Peak magnetograms. (This method is described in more detail in Section 3.3.3.) The timing of "F2" in Figure 3.1, and the behavior of the westward boundary of the coronal hole in particular, corresponds to the appearance of sustained concentrated flux at about the 85° longitude (shown boxed in Figure 3.2) for Carrington rotations 1874–1878. Also notable is the lack of concentrated flux in the area to the immediate east of the active longitude. The westward boundary of the coronal hole during this time holds steady at about the 45° longitude. The discrepancy in longitude between the flux sources and the coronal hole is ascribed to their separation in latitude. The flux locations in Figure 3.2 are in the vicinity of the activity belt around 13° S latitude, while the stackplot displays the coronal hole at 60° S.

The relationship between the active longitude and an F-mode can be described by considering flux transport on the photosphere. Concentrated flux (perhaps from a sunspot) will diffuse away from the area at which it emerged into the solar atmosphere. The motion of individual flux elements will follow a random walk across the surface according to the changing flows of the supergranular network. The elements are also subject to ordered transport, such as the solar rotation (which introduces shear between latitudes) and possibly meridional flows. The flux from a concentrated region is destined to be cancelled out by flux of the opposite polarity, or to spread out into a unipolar region possibly located some distance away from its origin. If concentrated flux were continually introduced at a single location over a time period sufficient for a stationary pattern to form, there would be a unipolar region which is (a) contiguous to the flux source, and (b) at rest relative to the continuing source. This paper claims that the F-mode corresponds to the situation where the unipolar region associated with the polar coronal hole extension becomes attached to, and sustained by, a source of continuous emergence: an active longitude. It necessarily rotates at the rate of the flux source, which may be faster than the rate at the latitude at which it is observed. In contrast, the S-mode corresponds to the case where flux sources are too ephemeral to bring large unipolar regions to rest in their frame. The following sections demonstrate the two observed modes according to quantified flux emergence as measured in Kitt Peak magnetograms, and the SNW model of the subsequent diffusion and transport of this flux.

3.3 The Zonal Model

Sheeley, Nash and Wang have developed a description of the formation and maintenance of unipolar flux regions according to flux eruptions and surface transport of flux elements by supergranular diffusion, differential rotation, and meridional flows. Using observed flux eruptions and numerical integration of the transport equations, they reproduce the general global distribution of flux over the course of a solar cycle, and they have convincingly modelled the behavior of CH1 (Wang & Sheeley 1993), the prototypical coronal hole observed and analyzed by Skylab (Timothy, Krieger, & Vaiana 1975). These successes encourage an application to the question of the bimodal rotation rates. In this section the transport equations are presented, reduced, and analytically solved to examine the import of flux eruption for the bimodal behavior.

3.3.1 Flux-Transport Equation

To investigate the observed behavior of the large-scale unipolar regions it is sufficient to describe the magnetic flux distribution on the photosphere. Although electrical conductivity is high in the solar atmosphere, and thus the plasma and magnetic field motions are strongly coupled, the mass density decreases quickly enough with height that the higher altitudes (i.e., the corona) cannot significantly affect the motions of the magnetic field at the photosphere. Below the photosphere, the plasma pressure is much stronger than the magnetic field pressures (i.e., $\beta_{plasma} \equiv \frac{8\pi p}{B^2} \gg 1$) so the evolution of the flux distribution on the solar surface is determined by lateral surface flows (via the strong coupling to the plasma) and the emergence of new flux.

The field distribution on a surface (such as the photosphere) is a scalar function. Even though the magnetic field is a vector field, only the component normal to the surface (B_r at the photosphere) is relevant, so the flux-transport equation is a scalar equation of time-evolution for the magnetic field's normal component. For simplicity, this scalar hereafter will be labelled B.

Expressing the surface flows together as a surface current Γ of B, the motion of flux about the surface is given by accounting:

$$\begin{aligned} S(\mathbf{x}, t) &= \frac{\mathrm{d}B}{\mathrm{d}t} \\ &= \partial_t B + \nabla \cdot \mathbf{\Gamma}, \end{aligned} \tag{3.1}$$

where $S(\mathbf{x}, t)$ is the flux source term as a function of position on the surface $\mathbf{x}$ and time t, and spatial operators like ∇ are understood to be in two dimensions on the surface. The surface current function can be given as

$$\mathbf{\Gamma}(\mathbf{x}, t) = -\kappa \nabla B + \mathbf{v} B. \tag{3.2}$$

The first term on the RHS represents "diffusion" down the concentration gradient by random-walk processes. The second term encompasses "organized" flows.

Leighton (1964) developed the idea that the solar supergranulation acts over time as a random-walk process on the photospheric magnetic flux, and that this effect can be described mathematically like the diffusion of "atoms" on a 2D surface. Hence, the diffusion term in Equation (3.2) is understood to represent supergranulation as a flux-transport mechanism. The coefficient κ is set by fitting the diffusion model to the effect of supergranulation on the Sun. Leighton suggested ~800-1600 $\mathrm{km^2\,s^{-1}}$ as a possible range of values for κ, based on estimates of the decay of localized magnetic bipoles. More recent work based on measurements of the motions of magnetic flux elements (e.g., $\kappa \approx$ 200–250 $\mathrm{km^2\,s^{-1}}$ in Hagenaar et al. 1999) and on modelling (e.g., $\kappa \approx$ 400–800 $\mathrm{km^2\,s^{-1}}$ in Wang, Nash, & Sheeley 1989) suggests more conservative numbers. For this paper, the diffusion coefficient was set to $\kappa = 1000\,\mathrm{km^2\,s^{-1}}$. This number was set high to compensate for the exclusion of poleward flows in the F.T.E. Sheeley, Nash, & Wang (1987) have demonstrated the importance of meridional transport terms for reproducing solar patterns with the flux-transport model, and their results indicate that poleward flows may be a necessary addition. It will be seen in Figure 3.4 that there is apparently a stronger meridional transport on the Sun than the model produces, so the choice of κ does not appear to err on the side of excess.

The most obvious organized flow on the photosphere is due to the latitudinal shear of differential rotation. Another possibility is meridional flow from the equator towards the poles. There is some evidence for the presence of such flows (c.f., Duvall 1979, Howard & Labonte 1981, and Topka et al. 1982). It is important that the flux-transport equation allow for some kind of meridional transport, usually a combination of diffusion and poleward drift which acts to retard the shears imposed by differential rotation, and Wang, Nash, & Sheeley (1989) found a good average fit to the behavior of the Sun by including a meridional flow of amplitude $10\,\mathrm{m\,s^{-1}}$.

Combining Equations (3.1) and (3.2) produces

$$\partial_t B = \kappa \nabla^2 B - \nabla \cdot (\mathbf{v} B) + S(\mathbf{x}, t). \tag{3.3}$$

The surface, its coordinate system, and the physics of $\mathbf{v}(\mathbf{x}, t)$ remain to be specified. To make the flux-transport equation analytically tractable, two simplifications are made at this point. (1) The photosphere is described by Cartesian coordinates on a planar surface. (2) The organized flow $\mathbf{v}(\mathbf{x}, t)$ is chosen to fit the differential rotation profile; no poleward meridional flows are included. The planar approximation will apply as long as the solution has length scales $\lambda \lesssim R_\odot$, where $R_\odot$ is the solar radius. The benefit of the second enumerated choice will be illustrated in Section 3.3.2, where it will be seen how the functional form of a poleward drift can complicate the search for a Green function.

These two approximations allow Equation (3.3) to be expressed as

$$\partial_t B = \kappa {\partial_x}^2 B + \kappa {\partial_y}^2 B - v_x \partial_x B + S(x, y, t), \tag{F.T.E.}$$

where the x-axis lies in the "azimuithal" direction, parallel to the equator, and the y-axis lies in the "meridional" direction, perpendicular to the equator. This is the specific form of the flux-transport equation (F.T.E.) for this analysis. The model includes diffusion of flux by supergranular flows, and latitudinal shear by differential rotation. The latter is described by a velocity vector which is everywhere parallel to the equator and only varies with latitude, i.e.,

$$\mathbf{v}(\mathbf{x}) = \mathbf{v}_{rot}(x, y) = v_x(y)\hat{\mathbf{x}}. \tag{3.4}$$

The functional form of $v_x(y)$ can be fitted to the observed differential rotation of the Sun. An adequate formula is

$$v_x(y) = v_0 - \frac{\Omega}{R} y^2, \tag{3.5}$$

where $R = R_\odot$, and v_0 and Ω are varied to produce a match to observations. Figure 3.3 matches this formula at 0° and 65° to the Snodgrass (1983) rotation rate for nonspot magnetic fields in the photosphere. The angular velocity is converted to a linear velocity on the Cartesian plane of the zonal model using the solar radius $R_\odot$ as the length scale. Using $R_\odot = 7.0 \times 10^5\,\mathrm{km}$, this leads to $v_0 = 45\,\mathrm{km\,s^{-1}}$ and $\Omega = 1.1 \times 10^{-5}\,\mathrm{s^{-1}}$.

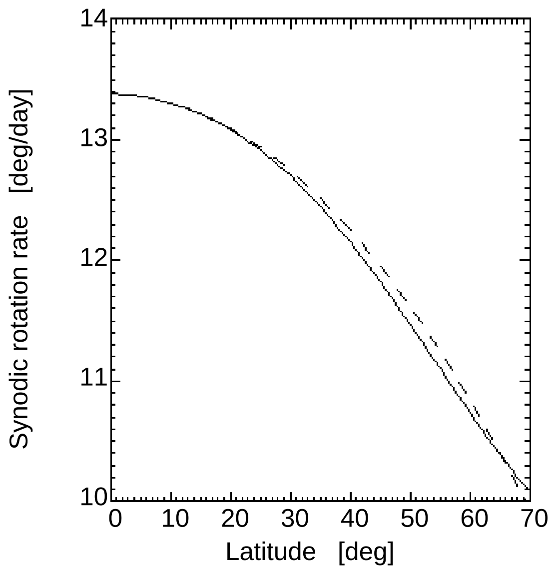

Figure 3.3: A comparison between the empirical Snodgrass (1983) rotation profile (*solid line*) and a parabolic fit like Equation (3.5) (*dashed line*). The parabolic fitting parameters $\{v_0, \Omega\}$ are fixed such that the curves match at 0° and 65°. For the latitudes of interest, the fit is good to about 1–2%, which is the approximate level of uncertainty on solar rotation measurements.

3.3.2 Zonal Moments of the Flux Distribution

A full numerical or analytic solution to the flux-transport equation (F.T.E.) would provide complete information on the scalar field B at all times t. However, the present goal is merely to understand a few characteristics of large-scale unipolar regions, such as their location, rotation, and approximate size and shape. This more limited set of information is readily obtained by solving for the low-order longitudinal, or "zonal", moments of the flux distribution, where the n-th moment of $B(x, y, t)$ is defined by integrals over the longitudinal coordinate x as

$$\langle x^n \rangle \equiv \frac{\int_{-\infty}^{\infty} x^n B(x,y,t)\,\mathrm{d}x}{\int_{-\infty}^{\infty} B(x,y,t)\,\mathrm{d}x}. \tag{3.6}$$

In this subsection, it will be shown how the zero-order moment can be solved using a Green function. This Green function can also be used to solve for the first- and second-order moments of the field. These three zonal moments are sufficient to describe the flux distribution from a point source with a Gaussian profile.

The unnormalized zero-order moment is the total latitudinal flux $\Phi(y,t)$, hereafter called the "zonal flux", where

$$\Phi(y,t) \equiv \int_{-\infty}^{\infty} B(x,y,t)\,\mathrm{d}x. \tag{3.7}$$

An equation for $\Phi(y,t)$ is found by integrating $\int$ (F.T.E.) $\mathrm{d}x$;

$$\int_{-\infty}^{\infty} [\partial_t B]\,\mathrm{d}x = \int_{-\infty}^{\infty} \left[\kappa {\partial_x}^2 B + \kappa {\partial_y}^2 B - v_x \partial_x B + S(x,y,t)\right] \mathrm{d}x, \tag{3.8}$$

which can be reduced by integration by parts and Equation (3.7) to

$$\partial_t \Phi = \kappa\, {\partial_y}^2 \Phi + \int_{-\infty}^{\infty} S(x,y,t)\,\mathrm{d}x \tag{3.9}$$

(where it is presumed that B and $\partial_x B$ both go to zero as $x \to \pm\infty$). For an impulsive point flux source at time $t = 0$,

$$S(x, y, t) = S_0\, \delta(x - x_0)\, \delta(y - y_0)\, \delta(t) \tag{3.10}$$

and Equation (3.9) can be rewritten in the form

$$\mathcal{L}\, \Phi = \left\{ \partial_t - \kappa \partial_y{}^2 \right\} \Phi = S_0\, \delta(y - y_0)\, \delta(t). \tag{3.11}$$

(The notation $\delta(z - z_0)$ indicates a Dirac delta function located at $z = z_0$.) Except for the constant factor of S_0, this is the form of the operator equation for a Green function, i.e.,

$$\mathcal{L}\, G(y, y_0; t, 0) = \delta(y - y_0)\, \delta(t). \tag{3.12}$$

The solution is the Green function for diffusion in one dimension:

$$G_{\mathrm{Diff}}(y, y'; t, t') = \frac{1}{\sqrt{4\pi\kappa\,(t - t')}}\, e^{-(y - y_0)^2/4\kappa(t - t')}\, \Theta(t - t')\, \Theta(t'), \tag{3.13}$$

and so

$$\begin{aligned} \Phi(y, t) &= S_0\, G_{\mathrm{Diff}}(y, y_0; t, 0) \\ &= \frac{S_0}{\sqrt{4\pi\kappa\, t}}\, e^{-(y - y_0)^2/4\kappa t}\, \Theta(t). \end{aligned} \tag{3.14}$$

(The step-functions $\Theta(t - t')$ and $\Theta(t')$ enforce causality for point sources at times t' where $0 \leq t' \leq t$.) The reader should not be surprised to discover that $\Phi(y, t)$ evolves only according to diffusion. A latitudinal shear cannot affect the zonal flux. This result (for a spherical surface) was previously demonstrated by Leighton (1964).

At this point, the rationale for omitting poleward flows can be clearly illustrated. It is presumed that the velocity $\mathbf{v}(\mathbf{x})$ is comprised of the differential rotation velocity $\mathbf{v}_{rot}(x,y)$, a vector which is everywhere parallel to the equator and only varies with latitude,

$$\mathbf{v}_{rot}(x,y) = v_x(y)\hat{\mathbf{x}}; \tag{3.15}$$

and the meridional poleward flow $\mathbf{v}_{pole}(x,y)$, a vector which is everywhere perpendicular to the equator and also only varies with latitude,

$$\mathbf{v}_{pole}(x,y) = v_y(y)\hat{\mathbf{y}}. \tag{3.16}$$

Referring to Equation (3.3), the divergence term can be written out as

$$\begin{aligned} \nabla \cdot (\mathbf{v}B) &= (\partial_x v_x + \partial_y v_y)B + (v_x \partial_x B + v_y \partial_y B), \\ &= (\partial_y v_y)B + (v_x \partial_x B + v_y \partial_y B). \end{aligned} \tag{3.17}$$

The first and third terms on the RHS are due to the poleward flow, and their inclusion in the velocity leads to two extra terms in the F.T.E. Equation (3.11) becomes

$$\left\{\partial_t - \kappa {\partial_y}^2 + v_y \partial_y + (\partial_y v_y)\right\} \Phi = S_0\, \delta(y - y_0)\, \delta(t). \tag{3.18}$$

The homogeneous equation has changed. The presence of the first-order partial derivative implies that the corresponding Green function cannot be G_{Diff}. In retrospect, omission of poleward flows has greatly simplified the search for a Green function solution.

The presumption to model the flux source function as a point source also has merit. First, this led to a natural solution by a Green function, and more complicated source functions can be described by a linear combination of such solutions. Second, there is a physical basis in that the greatest sources of photospheric flux are associated with sunspots, and appear in relatively small regions (compared to the solar radius) and with relatively high concentrations of flux (compared to the background level). The fitting of point sources to Kitt Peak magnetogram data is discussed in detail in Section 3.3.3.

The form of $\Phi(y,t)$ indicates a Gaussian profile across latitude. It seems reasonable to assume that the decaying point source will have a Gaussian-like profile across longitude as well. Such a profile has three free parameters, so the first three moments of the field should provide a sufficient approximation of the form

$$B(x,y,t) \simeq \frac{\Phi(y,t)}{\sqrt{2\pi\Delta x^2}}\, e^{-(x-\langle x\rangle)^2/2\Delta x^2}, \tag{3.19}$$

where Φ, $\langle x\rangle$, and Δx^2 are functions of y and t, and

$$\Delta x^2 = \langle x^2\rangle - \langle x\rangle^2. \tag{3.20}$$

This rendition of the magnetic flux distribution according to a Gaussian composed of the first three longitudinal moments is hereafter referred to as the "zonal model".

The first-order longitudinal moment follows from Equation (3.6);

$$\begin{aligned}
\langle x\rangle &= \frac{\int_{-\infty}^{\infty} xB(x,y,t)\,\mathrm{d}x}{\Phi(y,t)} \\
&= \frac{\int_{-\infty}^{\infty} (\xi+x_0)B(\xi,y,t)\,\mathrm{d}\xi}{\Phi(y,t)} \\
&= \frac{\int_{-\infty}^{\infty} \xi B(\xi,y,t)\,\mathrm{d}\xi}{\Phi(y,t)} + \frac{x_0\Phi(y,t)}{\Phi(y,t)} \\
&= \frac{f(y,t)}{\Phi(y,t)} + x_0, \qquad (3.21)
\end{aligned}$$

where

$$f(y,t) \equiv \int_{-\infty}^{\infty} \xi B(\xi,y,t)\,\mathrm{d}\xi. \qquad (3.22)$$

The variable $\xi \equiv x - x_0$ is introduced to symmetrize the integral about x_0. Next, the first-order moment equation is derived by integrating $\int x\,(\text{F.T.E.})\,\mathrm{d}x$.

$$\int_{-\infty}^{\infty} x\,[\partial_t B]\,\mathrm{d}x = \int_{-\infty}^{\infty} x\left[\kappa{\partial_x}^2 B + \kappa{\partial_y}^2 B - v_x\partial_x B + S(x,y,t)\right]\mathrm{d}x,$$

$$\partial_t f + x_0\partial_t\Phi = \kappa{\partial_y}^2 f + x_0\kappa{\partial_y}^2\Phi + v_x\Phi + x_0\,S_0\,\delta(y-y_0)\,\delta(t), \qquad (3.23)$$

where it is assumed that $\{B, xB, \partial_x B, x\partial_x B\}$ all go to zero as $x \to \pm\infty$. Three more terms can be eliminated by Equation (3.11), leaving

$$\partial_t f = \kappa{\partial_y}^2 f + v_x\Phi. \qquad (3.24)$$

The homogeneous part of Equation (3.24) is identical to that of Equation (3.11), so its Green function is the same. Thus the inhomogeneous solution to Equation (3.24) is readily found:

$$f(y,t) = \int_{-\infty}^{\infty}\int_{-\infty}^{\infty} G(y,y',t,t')\left[v_x(y')\Phi(y',t')\right]\mathrm{d}y'\mathrm{d}t'. \tag{3.25}$$

The functions $G(y,y',t,t'), v_x(y')$, and $\Phi(y',t')$ have been completely specified, and the integral is easily solved. The solution for $f(y,t)$ is inserted into Equation (3.21) to produce a closed-form solution for the first moment;

$$\langle x\rangle(y,t) = x_0 - \frac{1}{3}\frac{\Omega}{R}t\left[\kappa t + y^2 + yy_0 + {y_0}^2\right]. \tag{3.26}$$

Following the same procedure, the second-order moment of the magnetic field can be determined. The moment:

$$\begin{aligned}\langle x^2\rangle &= \frac{\int_{-\infty}^{\infty} x^2 B(x,y,t)\,\mathrm{d}x}{\Phi(y,t)}\\ &= \frac{g(y,t)}{\Phi(y,t)} + 2x_0\frac{f(y,t)}{\Phi(y,t)} + {x_0}^2,\end{aligned} \tag{3.27}$$

where

$$g(y,t) \equiv \int_{-\infty}^{\infty} \xi^2 B(\xi,y,t)\,\mathrm{d}\xi. \tag{3.28}$$

The integral $\int x^2\,(\mathrm{F.T.E.})\,\mathrm{d}x$ after integration by parts and eliminating terms with

Equations (3.11) and (3.24):

$$\partial_t g = \kappa {\partial_y}^2 g + 2\left[\kappa + v_x\left(\langle x\rangle - x_0\right)\right]\Phi, \tag{3.29}$$

where the set $\{B, xB, x^2B, \partial_x B, x\partial_x B, x^2\partial_x B\}$ is presumed to go to zero in the limit $x \to \pm\infty$. Equation (3.29) has the same homogeneous structure as Equations (3.11) and (3.24), and so can be solved for $g(y,t)$ (and thus $\langle x^2\rangle$) with the same Green function. The importance of the second-order moment $\langle x^2\rangle$ extends no farther here than its contribution to Δx^2 according to Equation (3.20), which in turn is useful for approximating the flux distribution according to Equation (3.19).

3.3.3 Source Function Based on Magnetograms

In Section 3.3.2 a Gaussian approximation of the flux-distribution was developed with the first three moments of the field. The input to this model is represented by the flux source function $S(\mathbf{x},t)$ which describes the appearance of new flux on the surface according to the flux "conservation" equation (3.1). The approximation formula (3.19) was constructed for an impulsive point source. Since the evolution equations are linear, a more complicated source function can be described with a superposition of such point sources over space and time.

Synoptic charts of Kitt Peak magnetograms were analyzed for appearances of new, concentrated flux. A subset of pixels from each chart, identified as locations of high magnetic field, were used to represent point sources containing the predominant amount of new concentrated flux. The threshold criterion for selecting pixels was a minimum value of 800 G. (This value was chosen to compromise between collecting a manageably low number of pixels and adequately representing the spatial extent and shape of new flux regions.) Although background levels of flux were generally insignificant in comparison to new flux, these levels were estimated for each Carrington rotation (from the evolution of flux introduced in earlier rotations) and subtracted from the measured values of new flux.

The flux sources were grouped into bipoles. Unipolar subsets for which no oppositely polar subset could be found were discarded. Where the total (signed) flux in a bipolar subset was not equal to zero, the pixel values in the pole of lesser absolute flux were multiplied by a uniform factor such that the total bipolar flux was zero. The latter correction was necessary; it was discovered that otherwise the net imbalance of (selected) flux in each hemisphere quickly grew in opposition to the solar dipole field. (I.e., the "leading" spot polarity was dominant.) At this point in the solar activity cycle the solar dipole had already formed and has remained stable well past the appearance of the current activity cycle's flux, so this result presented a strong inconsistency.

The flux distribution at time t could then be calculated according to the present model from the empirically-derived point sources at times t' where $0 \leq t' \leq t$. The results of this procedure are presented in the next Section to explain the F-mode behavior.

3.4 Results

The approximation method described in the preceding Section can be used to construct maps similar to the synoptic charts made from magnetograms. The flux-distribution was solved on an area with an "azimuthal" length of $2\pi R_\odot$ and a "meridional" width of $\pi R_\odot$. The $x = \pm\pi R_\odot$ ends were connected to avoid loss of significant flux. The Gaussian "amplitudes" of the diffusing point sources, and hence their influence on the net distribution, dropped off quickly with distance relative to the curvature length-scale of the Sun ($R_\odot$), so this choice of surface did not appear to present serious curvature concerns. Figure 3.4 compares a synoptic chart constructed in this manner with some Kitt Peak data. In both plots, areas of weak and mid-range field strength have been assigned saturation values on the greyscale in order to more clearly indicate the extent of unipolar flux regions. The modelled example was produced from ten preceeding rotations' worth of point source data. This method appears to reflect the measured distribution of flux in general. However, the zonal model fails to reproduce as large an amount of positive (white) flux near the south polar cap; this is probably due to the model's neglect of organized poleward flows.

Figure 3.5 compares a stackplot made from Kitt Peak magnetograms with a stackplot made from the psuedo-magnetograms produced by the field approximations, such as the one in Figure 3.4. The stackplot shows only a latitudinal strip of the Sun over 720° of longitude, so features appear twice. Each strip going down the stackplot represents one solar rotation. For Figure 3.5, flux magnitudes were suppressed so only the polarity is indicated. Figure 3.5(a) was constructed from smoothed Kitt Peak data. This picture helps to illustrate how well the method models the behavior of the unipolar region associated with the south polar coronal hole extension (PCHE), which appears as the wide black lane. Again, the model reproduces the qualitative behavior of the data. In particular, at around Rotation #1875, new negative (black) flux is seen to appear on the righthand (western) boundary of the region. This has the effect of "fixing" this boundary at an almost constant longitude for several rotations. The extra flux also allows the opposite boundary to continue to expand. The swelling is less significant in the Kitt Peak data at this latitude, but the reader may discern that the "intensity" of black (i.e., the amount of negative flux) increases.

Why does Figure 3.5 show the behavior of the PCHE at 35° S instead of at 60° S? As can be discerned in Figure 3.4(a), the flux distribution in the southern hemisphere is relatively axisymmetric (i.e., all negative) at latitudes poleward of about 35°. Nevertheless, the longitude of the PCHE at 60° S will follow the longitude of the major non-axisymmetric flux distribution (that is, the extension of the negative region towards the equator), at latitudes closer to the equator. Therefore, it is assumed that the most poleward latitudes containing a non-axisymmetric distribution should provide a reasonable proxy for the behavior of the coronal hole at more poleward latitudes.

The relevance of the active longitude is investigated in Figure 3.6. These small stackplots are both produced from the zonal model in a fashion identical to that of Figure 3.5(b), excepting the source function. For part (a), the flux source function

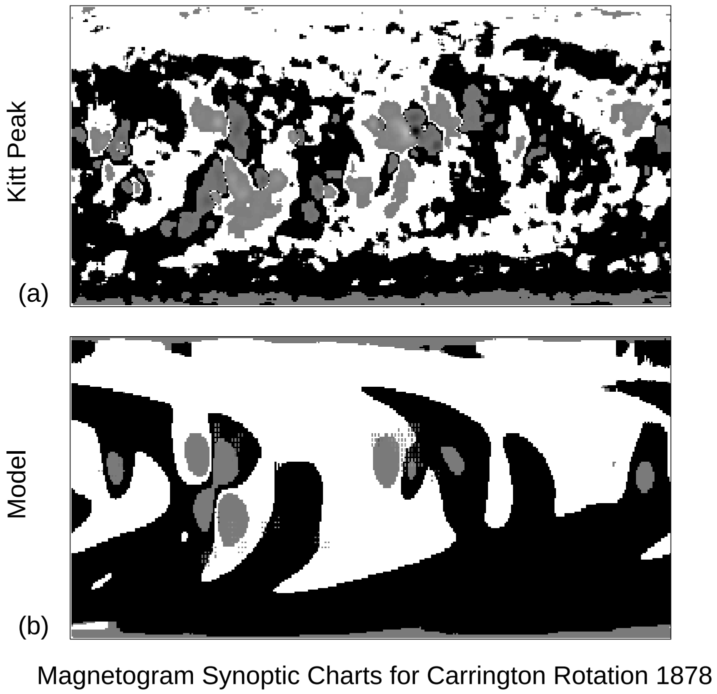

Figure 3.4: *(a)* A synoptic chart of Kitt Peak magnetogram data. The data was smoothed with a boxcar width of 5 pixels. *(b)* A synoptic chart for the same rotation produced from the approximation model described in this paper. No smoothing was imposed. White and black regions indicate positive and negative flux, respectively. The scaling emphasizes weak and mid-range field strengths to locate unipolar flux areas. Grey areas are scaled differently and indicate regions of greatest flux concentration.

only includes input from flux concentrations identified with the active longitude (see Figure 3.2), starting with Carrington Rotation #1874. (The single flux source at a nearby longitude in Rotation #1873 is also included as a reference point for the PCHE.) This figure shows how the zonal model reproduces the "fast" mode for the time period corresponding to the phase labelled "F2" in Figure 3.1. The characteristics previously ascribed to the "fast" mode in the PCHE behavior are discernable here. (1) A wide pattern is formed. (2) The righthand (western) boundary remains at the same approximate longitude. Although it is not apparent in the scaling of this figure, the longitudinal center of the region, weighted by flux magnitude, also remains close to a constant longitude. (3) The pattern is established relatively quickly, i.e., within 2–3 rotations.

Part (b) uses all of the flux sources from the same rotations *except* for those sources associated with the active longitude, so the behavior of the region is illustrated in the absence of the identified active longitude. In contrast to Figure 3.6(a), the negative unipolar region does not significantly change in width or rotation rate. This behavior replicates the "slow" mode as the normal behavior of the region in the presence of flux sources randomly distributed in time, and without the flux injection from a continual source at an active longitude. As a result, this model predicts that the "F2" mode would not have appeared in Figure 3.1 if the active longitude had not been present.

This section establishes (1) that the methodology can sufficiently describe the flux distribution on the solar surface; (2) that the active longitude produces a stationary unipolar pattern with the correct location and shape, on the timescale of about two

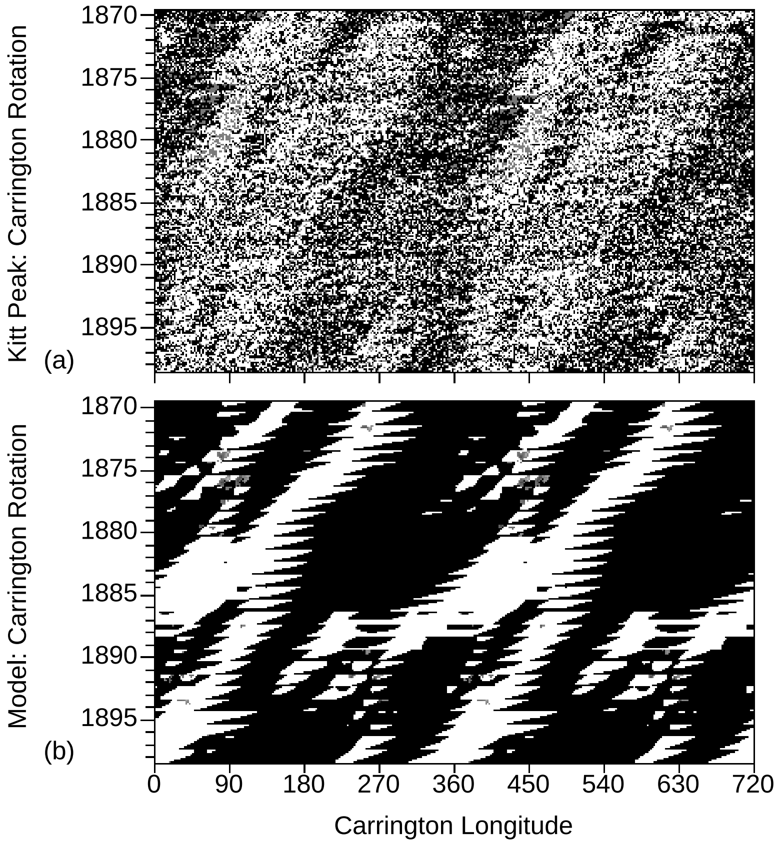

Figure 3.5: Stackplots for 35° S constructed from magnetogram synoptic charts, such as those shown in Figure 3.4. *(a)* Kitt Peak data which has been smoothed and scaled to emphasize weaker fields. *(b)* Results for the zonal model which have been similarly scaled.

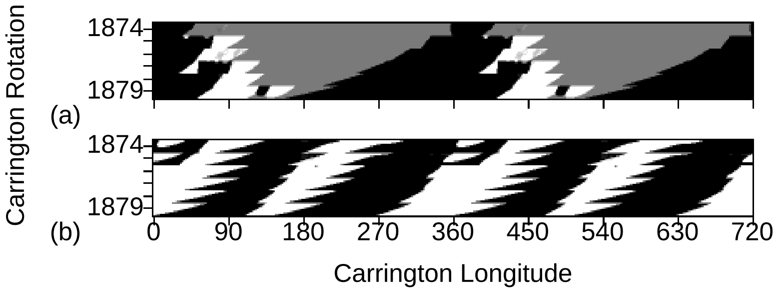

Figure 3.6: Stackplots for 35° S constructed from magnetogram synoptic charts for the time period corresponding to the "F2" example. Both stackplots were produced from the zonal model. *(a)* Flux pattern formed using only the sources associated with the active longitude. Here the grey region indicates insignificant flux levels. *(b)* Flux pattern formed by all sources *except* those associated with the active longitude.

rotations at a given latitude; and (3) that the existence of the F-mode requires the presence of the active longitude.

3.5 Discussion

It is observed in the declining phase of solar activity cycle 22 that the south polar coronal hole extension alternated between two phases which are described mainly by shape and rotation rate. It has been shown that one phase (the F-mode) is dependent upon the presence of an active longitude of concentrated flux eruption, and that the other phase (the S-mode) predominates in the absence of such an active longitude. Hence, an understanding of this bimodal nature of the coronal rotation rate must refer to an investigation of the longitudinal distribution of flux eruptions in general, and a study of active longitudes especially.

The result that the flux source term $S(\theta, \Phi, t)$ can strongly affect large-scale flux patterns is recognized and discussed in the SNW model. It is treated there in a general way. Its effect in their study of Skylab's CH1 (Wang & Sheeley 1993) is implicit (and hence somewhat hidden) in their numerical analysis. This chapter attempts to extend their analytic discussion of $S(\theta, \Phi, t)$ by connecting a clear, qualitative variation with its definite effect upon a large-scale pattern.

SNW also discuss how rigidly rotating unipolar patterns form at latitudes above the activity belt as the alternating curved stripes from decayed active regions. These patterns are supported in a balance between latitudinal shear and meridional transport via diffusion and possibly poleward flows. The appearance of new flux sources can disrupt this rigid rotation as the field in their vicinity will naturally be influenced to follow their differential rotation profile. Hence, flux eruptions are expected to cause the unipolar regions to depart from rigid rotation. In the case of an active longitude of sufficient duration however, a stationary and rigidly rotating pattern is *supported* by a strong source signal. Ultimately though, this is the case that proves their rule. Once the domineering active longitude vanishes, the unipolar pattern finds itself in a state of imbalance between the latitudinal shear and meridional transport. Differential rotation will ensue as the pattern migrates again towards homeostasis, according to the SNW description.

The zonal model provides a sufficiently good approximation to reproduce the general behavior of the observed phases, but more sophisticated analysis would probably require a numerical approach (c.f., Sheeley, Nash, & Wang 1987). Two significant approximations of the zonal model are the absence of a poleward flow and the use of a non-spherical surface; including either greatly complicates the analytic discussion. As discussed in Section 3.3.2, the functional form of a poleward flow would change the homogeneous equations for the first and second longitudinal moments; as a consequence, the Green function $G_{\mathrm{D}iff}$ could not be used to solve for all of them. The F.T.E. would clearly be trickier to deal with on a spherical surface. Although the flux distribution across the entire solar surface is modelled in this chapter, the contribution from each point source is generally only significant to regions within a distance $d \lesssim R_{\odot}$, so it is presumed that the solar curvature has minimal impact on the solution. However, spherical equations would be readily handled in a numerical analysis.

Apart from issues of approximation, there are several interesting directions in which this work could be extended. Only the "F2" case example is fully explored here; several other S and F-modes occurred in the same time period which should be modelled to more firmly establish the argument of active longitudes. It is also possible that the bimodal phenomenon can only occur in the declining phase of the solar activity cycle, when it is possible for large-scale unipolar regions to develop stationary behavior at latitudes well away from the activity belt. Active longitudes and PCHEs could be studied at other times in the cycle.

CHAPTER 4

AXIAL FIELDS IN QUIESCENT PROMINENCES

4.1 Introduction

Solar prominences are coronal magnetic structures in which relatively cool (5000–10,000 K; c.f., Hirayama, Nakagomi, & Okamoto 1979 and Heasley & Milkey 1983) and dense (10^{11} e^{-} cm^{-3}; c.f., Landman 1985 and Foukal, Hoyt, & Gilliam 1986) plasma is suspended at coronal heights (10^4–10^5 km) above the photosphere. The surrounding corona is about 100 times hotter and more rarefied, so the prominence material must be thermally shielded from the corona by its magnetic fields. Prominences are invariably located along segments of polarity inversion lines (PIL) which separate regions of positive and negative flux through the solar surface. Some prominences are associated with the sunspot latitudes. This type is short-lived and migrates equatorwards with the sunspots over the course of the solar activity cycle. Other prominences form poleward of the activity belt and move to higher latitudes. (The polar crowns are comprised of such prominences which have migrated to the boundaries of the polar coronal holes.) This type of prominence may last for days or even weeks and is

Figure 4.1: *(a)* The *observed* direction of axial fields in quiescent prominences for each hemisphere and relative to the polarity distribution of the surface flux. *(b)* The sense of shear for arcade lines over a polarity inversion line (PIL) as produced by Model A. Note that the components of sheared field along the polarity inversion lines agree with the sense of the axial fields in (a). This figure is based on Figure 1 of van Ballegooijen & Martens (1990), with the notable exception that the pair of PILs in each hemisphere represent young, poleward-migrating prominences, and do *not* describe polar crown prominences.

described as “quiescent”.

The magnetic fields of prominences projected above the solar limb can be measured by the Zeeman and Hanle effects (Leroy 1989). The results indicate that these fields are mostly horizontal with components parallel (axial) and perpendicular (transverse) to the long axis of the prominence (Athay et al. 1983; Querfeld et al. 1985). The overall field is close to axial, usually at an angle of 15° to 30° with respect to the prominence axis (e.g., Tandberg-Hanssen & Anzer 1970; and Leroy, Bommier, & Sahal-Brechot 1984). Much has been made of the direction of the transverse fields in the discrimination between prominence models, however, Rust (1967) and others later (c.f., Leroy, Bommier, & Sahal-Brechot 1984) point out that the direction of the axial fields also imposes constraints on the nature of prominence formation.

The direction of the axial field $\hat{\mathbf{b}}$ obeys a hemispheric dependence (illustrated in Figure 4.1.a) such that $\hat{\mathbf{b}} = \pm\hat{\mathbf{n}} \times \hat{\mathbf{r}}$, where the plus sign applies in the northern hemisphere (and minus in the southern). The vector $\hat{\mathbf{n}}$ points across the PIL from the positive to the negative side, and $\hat{\mathbf{r}}$ points radially outwards from the Sun; the vector $\hat{\mathbf{n}}$ generally alternates with the solar activity cycle.

As a result of the high electrical conductivity of the solar atmosphere, the magnetic field is "tied" to the plasma and at the photosphere the plasma motion dictates the motion of the field. Hence, shearing flows on and below the surface will rotate fields initially transverse to become axial. The solar differential rotation (i.e., the latitudinal gradient of the rotation) produces shear flows at the surface and is a natural candidate for explaining the hemispherical dependence. However, van Ballegooijen & Martens (1990) demonstrated how an arcade, initially constructed of potential fields with the PIL running east-west, which is sheared by differential rotation will acquire an axial component which has the *opposite* direction to the observed direction of axial fields in solar quiescent prominences.

They proposed two mechanisms which utilize the differential rotation to produce axial fields which match observations. In their first solution (hereafter, Model A), the PIL must be rotated by the shear by more than 90°. They discounted this idea on the grounds that quiescent prominences (and polarity inversion lines) at high latitudes are almost always oriented east-west and are not observed to rotate through large angles. Their second solution (hereafter, Model B) invokes subsurface differential rotation and a complicated process which involves three stages of reconnection and the eruption of a heretofore unobserved helical field.

This paper argues that polarity inversion lines of prominences can indeed be rotated through angles greater than 90° when they are associated with the dispersal of active regions, and hence the simpler Model A should be reconsidered.

4.2 Neutral line rotation

The creation of an axial field component via the differential rotation is modelled in van Ballegooijen & Martens (1990); their case for initial angle $\beta_0 > 90°$ is illustrated in Figure 4.2. In this description, the field lines are initially potential in an arcade formation at right angles to the PIL (Figure 4.2.a). The field is "line-tied" to the motion of the photosphere. The rotational shear in the local frame of reference is given with the surface velocity:

$$v_x = -\omega y, \qquad v_y = 0, \tag{4.1}$$

where the x-axis runs east-west and the y-axis runs north-south, and ω is the radially outward component of vorticity associated with the differential rotation ($\omega > 0$ in the northern hemisphere).

The PIL begins at an angle β_0 with respect to a line of constant latitude and as time advances $\beta(t) \to 0$. The angle α between the field lines and the PIL begins at 90° and also becomes more acute with the passage of time, i.e., the initially transverse

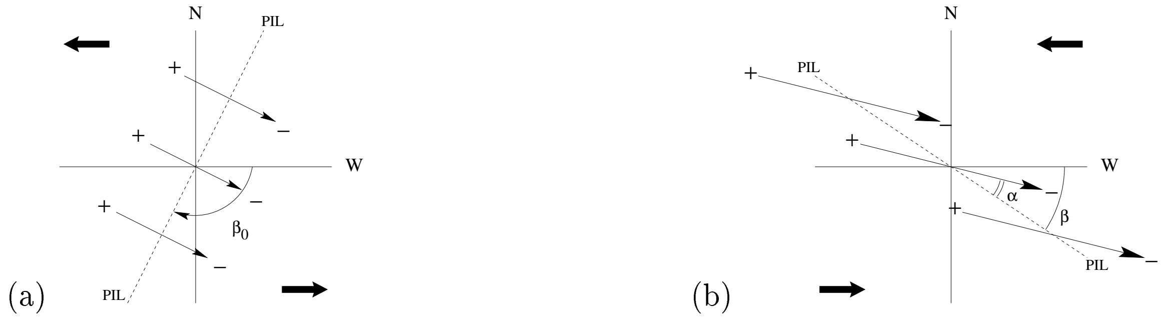

Figure 4.2: *(a)* Initial configuration of a potential field arcade over a polarity inversion line (PIL) with symmetry along the axis. The thick arrows indicate the direction of a shear appropriate to the northern solar hemisphere. The angle β_0 between the PIL and a line of constant latitude begins at a value greater than 90°. *(b)* The arcade at a later time where the fields have moved according to a linear surface shear. The PIL has rotated, and the angle α between the PIL and the fields is no longer equal to 90°, which indicates there is an axial component. This figure is based on Figure 3 of van Ballegooijen & Martens (1990).

fields are sheared such that they gain an axial component (Figure 4.2.b). Figure 4.1.b indicates the direction of the sheared fields in each hemisphere. A comparison with Figure 4.1.a confirms that this mechanism produces the observed direction of axial fields *for young, poleward-migrating prominences.* This mechanism of neutral line rotation is not argued here to produce the correct axial fields for the older population of prominences which form the polar crowns. The pair of PILs in each hemisphere of Figure 4.1 is intended to indicate the arrangements for alternate advancing fronts of quiescent prominences.

This result is mathematically described in van Ballegooijen & Martens (1990) as a function of the initial angle β_0 and time. For the case where $0° < \beta_0 < 45°$, neutral line rotation gives the *incorrect* orientation of the axial component. For the intermediate range of initial angles where $45° < \beta_0 < 90°$, the arcade shear gives the correct axial orientation at early times $t < t_1$, and the incorrect orientation at later times $t > t_1$. The reversal time t_1 is given in their Equation (7):

$$t_1 = \omega^{-1}(\tan\beta_0 - \cot\beta_0). \tag{4.2}$$

They point out that for β_0 just under 90°, t_1 might be long enough for a prominence to form while the axial fields still have the correct direction. Once the prominence forms, it is believed that the axial "correctness" would be frozen in, so for short prominence formation time scales, the range of favorable initial angles may extend below 90°.

This mechanism (Model A) was deemed implausible by van Ballegooijen & Martens (1990) since they believed that such large initial tilts of the PIL were not observed. In fact, there is a large population of polarity inversion lines which starts with this magnitude of tilt. Active regions arise as two concentrations of oppositely-polarized magnetic flux. Described as "Joy's Law" (Hale et al. 1919), the long axis of this bipole is, on average, tilted with respect to latitude such that the leading polarity is closer to the equator than the following polarity (for a statistical treatment, see Fisher, Fan, & Howard 1995). The PIL begins as the perpendicular bisector of the long axis and thus must be at an angle $\beta_0 > 90°$. Figure 4.3 displays the dispersal of flux from a bipole according to a flux-transport model which includes a parabolic rotation profile and diffusion. The center of the bipole begins at 15° N with an initial tilt angle of 10° towards the equator. This pattern is regularly observed in magne-

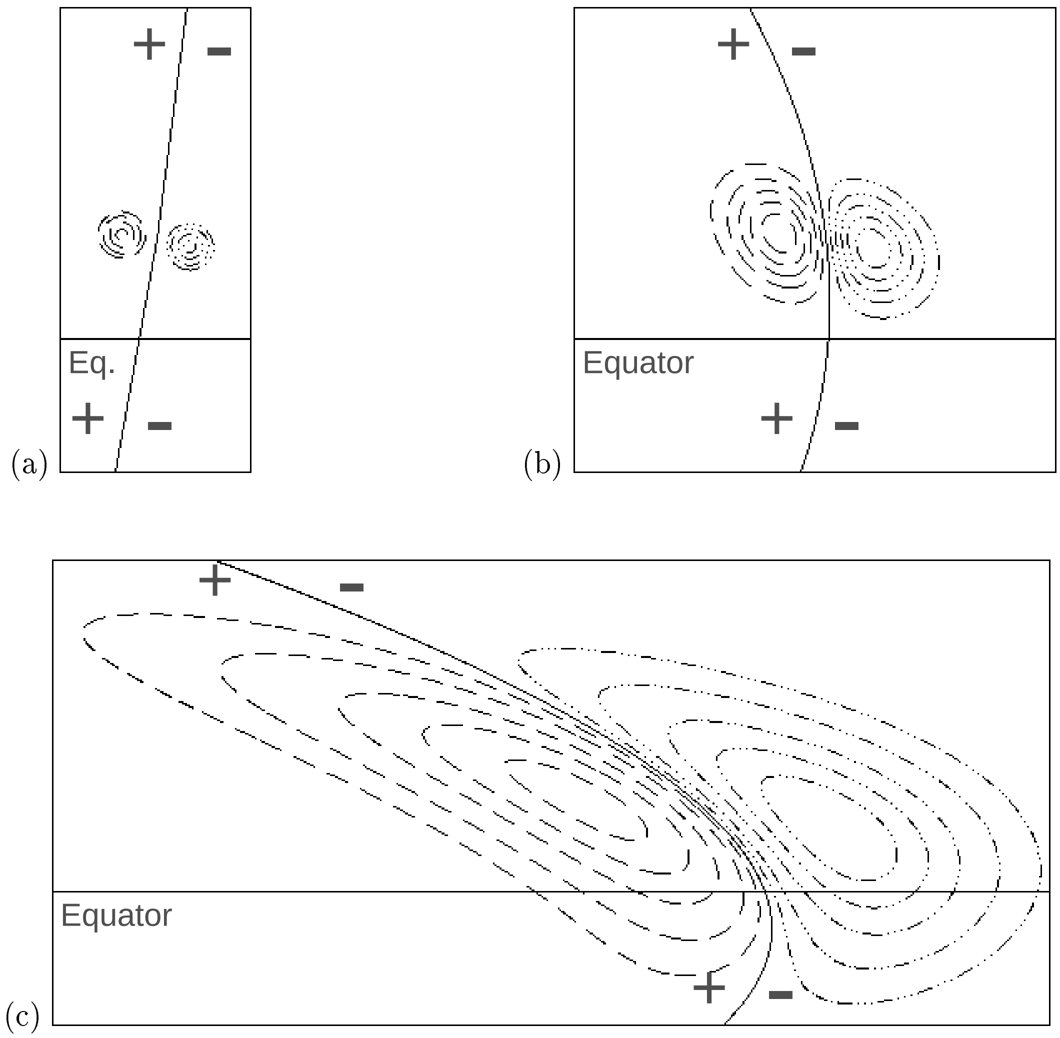

Figure 4.3: Evolution of a flux bipole from two point sources of opposite polarity according to diffusion and parabolic shear across latitudes. The positive (+) polarity is marked by long dashes, the negative (−) by dash-dot-dot-dot. The curved solid line indicates the polarity inversion line (PIL). The horizontal solid line indicates the solar equator. Parameters are fit to solar values of differential rotation and diffusion and the solution models the decay of an active region at *(a)* 0.1, *(b)* 1.0, and *(c)* 5.0 solar rotations (see Chapter 3). Contour levels are shown to indicate shape and are not similarly scaled between figures. Note the rotation of the PIL.

tograms, and was modelled as early as 1964 by Leighton (Leighton 1964). The PIL is observed to rotate over time. Statistically, most of the large regions of leading polarity at high latitudes will arrive through this configuration. Insofar as the fields retain their topological connectivity to the following region of opposite polarity, the correct axial fields should be formed in the conceptual manner of Model A.

4.3 Discussion

The second solution of van Ballegooijen & Martens (1990) for the formation of axial fields with the observed direction was based on the observation that for small β_0, the *subsurface* sections of the arcade are sheared to have the correct axial component. Models such as that of Priest, van Ballegooijen, & Mackay (1996) are based on this mechanism. In the preparation phase of their model, the sheared arcades would be expected to show axial components with the incorrect orientation; however, they argue that the coronal fields intermittently relax to a potential configuration on a timescale of days according to the tearing mode instability.

In contrast, Model A of van Ballegooijen & Martens (1990) produces the correct axial fields almost immediately, although the initial field configuration of active regions is never that of a uniform arcade with symmetry along the axis. The argument that the shear of active regions produces the correct axial fields requires further investigation into the efficiency with which the initially concentrated flux diffuses outward along the polarity inversion line to form the sorts of unipolar regions between which prominences are found. The assumption that the fields are “line-tied” may also need deeper consideration. It is apparent that magnetic reconnection takes place in the solar atmosphere, and is probably a key mechanism in the evolution of the largest coronal structures (c.f., Wang & Sheeley 1993, on the rigid rotation of coronal holes). Reconnection can allow sheared fields to relax, which could greatly impact the progression of Model A. On the other hand, reconnection is probably necessary to construct a prominence in the inverse topology (Pneuman 1983; van Ballegooijen & Martens 1989). The question is not whether reconnection takes place, but whether it significantly changes the connectivity of the local fields to regions located far away from the PIL, or allows the coronal fields to relax to their potential state on the timescales associated with the formation of filament channels. Active region structures are observed to resist complete relaxation, sometimes for several solar rotations (i.e., months), so the question remains open on how well the axial fields can be maintained in Model A under solar conditions.

Joy’s Law states that there is a statistical tendency for active regions to have tilt angles such that the leading polarity is closer to the equator than the following one. However, there is a lot of scatter in the distribution of observed tilt angles, and a non-negligible part of the population corresponds to initial angles $\beta_0 < 90°$. As mentioned earlier, angles β_0 just under 90° can still lead to correctly oriented axial fields if the prominences form early enough to freeze the axial direction. The small number of quiescent prominences which are observed to violate the hemispheric rule for axial direction are predicted to correspond to the small population of active regions which go against Joy's Law, i.e., which supply initial angles β_0 too much less than 90°. A statistical comparison of these two populations could be made to test this hypothesis. Conversely, an assumption of correlation could be used to estimate t_1, the prominence formation time.

BIBLIOGRAPHY

BIBLIOGRAPHY

Aschwanden, M. J., Lim, J., Gary, D. E., & Klimchuk, J. A. 1995, ApJ, 454, 512

Athay, R. G., Querfeld, C. W., Smartt, R. N., Deglinnocenti, E. L., & Bommier, V. 1983, Sol. Phys., 89, 3

Devore, C. R., Sheeley, J., N. R., & Boris, J. P. 1984, Sol. Phys., 92, 1

Duvall, J., T. L. 1979, Sol. Phys., 63, 3

Fisher, G. H., Fan, Y., & Howard, R. F. 1995, ApJ, 438, 463

Fisher, R., & Sime, D. G. 1984, ApJ, 287, 959

Foukal, P., Hoyt, C., & Gilliam, L. 1986, ApJ, 303, 861

Hagenaar, H. J., Schrijver, C. J., Title, A. M., & Shine, R. A. 1999, ApJ, 511, 932

Hale, G. E., Ellerman, F., Nicholson, S. B., & Joy, A. H. 1919, ApJ, 49, 153

Hansen, R. T., Hansen, S. F., & Loomis, H. G. 1969, Sol. Phys., 10, 135

Heasley, J. N., & Milkey, R. W. 1983, ApJ, 268, 398

Hirayama, T., Nakagomi, Y., & Okamoto, T. 1979, in Physics of solar prominences; Proceedings of the Colloquium, Oslo, Norway, August 14-18, 1978. (A79-46076 20-92), 48

Hoeksema, J. T. 1984, Ph.D. thesis, Stanford Univ., CA.

Hoeksema, J. T., & Scherrer, P. H. 1987, ApJ, 318, 428

Horne, J. H., & Baliunas, S. L. 1986, ApJ, 302, 757

Howard, R. 1984, ARA&A, 22, 131

Howard, R., & Labonte, B. J. 1981, Sol. Phys., 74, 131

Kozuka, Y., Watanabe, T., Kojima, M., Ohyama, M., & Saito, T. 1994, in Proceedings of Kofu Symposium, Kofu, Japan, Sept. 6-10, 1993, p.359-362., 359

Landman, D. A. 1985, ApJ, 290, 369

Leighton, R. B. 1964, ApJ, 140, 1547

Leroy, J. L. 1989, in Dynamics and structure of quiescent solar prominences; Proceedings of the Workshop, Palma de Mallorca, Spain, (A89-51201 22-92). (Kluwer Academic Publishers), 77

Leroy, J. L., Bommier, V., & Sahal-Brechot, S. 1984, A&A, 131, 33

Morrison, M. 1994, YOHKOH Analysis Guide (Lockheed Palo Alto Research Laboratory)

Nash, A. G., Sheeley, J., N. R., & Wang, Y. M. 1988, Sol. Phys., 117, 359

Parker, G. D., Hansen, R. T., & Hansen, S. F. 1982, Sol. Phys., 80, 185

Pneuman, G. W. 1983, Sol. Phys., 88, 219

Press, W. H., Teukolsky, S. A., Vetterling, W. T., & Flannery, B. P. 1992, Numerical Recipes in FORTRAN (2nd ed.) (Cambridge University Press)

Priest, E. R., van Ballegooijen, A. A., & Mackay, D. H. 1996, ApJ, 460, 530

Querfeld, C. W., House, L. L., Smartt, R. N., Bommier, V., & Deglinnocenti, E. L. 1985, Sol. Phys., 96, 277

Rust, D. M. 1967, ApJ, 150, 313

Scargle, J. D. 1982, ApJ, 263, 835

Sheeley, J., N. R., Nash, A. G., & Wang, Y. M. 1987, ApJ, 319, 481

Sime, D. G., Fisher, R. R., & Altrock, R. C. 1989, ApJ, 336, 454

Snodgrass, H. B. 1983, ApJ, 270, 288

Tandberg-Hanssen, E., & Anzer, U. 1970, Sol. Phys., 15, 158

Timothy, A. F., Krieger, A. S., & Vaiana, G. S. 1975, Sol. Phys., 42, 135

Topka, K., Moore, R., Labonte, B. J., & Howard, R. 1982, Sol. Phys., 79, 231

Tsuneta, S., Acton, L., Bruner, M., Lemen, J., Brown, W., Caravalho, R., Catura, R., Freeland, S., Jurcevich, B., & Owens, J. 1991, Sol. Phys., 136, 37

van Ballegooijen, A. A., & Martens, P. C. H. 1989, ApJ, 343, 971

van Ballegooijen, A. A., & Martens, P. C. H. 1990, ApJ, 361, 283

Wang, Y. M., Nash, A. G., & Sheeley, J., N. R. 1989, Science (ISSN 0036-8075), vol. 245, Aug. 18, 1989, p. 712-718. Research supported by the U.S. Navy., 245, 712

Wang, Y. M., & Sheeley, J., N. R. 1993, ApJ, 414, 916

Wang, Y. M., Sheeley, J., N. R., Hawley, S. H., Kraemer, J. R., Brueckner, G. E., Howard, R. A., Korendyke, C. M., Michels, D. J., Moulton, N. E., Socker, D. G., & Schwenn, R. 1997, ApJ, 485, 419

Wang, Y. M., Sheeley, J., N. R., Nash, A. G., & Shampine, L. R. 1988, ApJ, 327, 427

Weber, M. A., Acton, L. W., Alexander, D., Kubo, S., & Hara, H. 2000, Sol. Phys., in press.